

FORBIDDEN LINE EMISSION FROM TYPE IA SUPERNOVA REMNANTS CONTAINING BALMER-DOMINATED SHELLS

CHUAN-JUI LI (李傳睿)¹, YOU-HUA CHU (朱有花)^{1,2}, JOHN C. RAYMOND³,
BRUNO LEIBUNDGUT⁴, IVO R. SEITENZAHL⁵, GIOVANNI MORLINO⁶

¹ Institute of Astronomy and Astrophysics, Academia Sinica, No. 1, Sec. 4, Roosevelt Rd., Taipei 10617, Taiwan
cjli@asiaa.sinica.edu.tw, yhchu@asiaa.sinica.edu.tw

² Department of Astronomy, University of Illinois at Urbana-Champaign, 1002 West Green Street,
Urbana, IL 61801, U.S.A.

³ Harvard-Smithsonian Center for Astrophysics, 60 Garden Street, Cambridge, MA, 02138, USA

⁴ European Southern Observatory, Karl-Schwarzschild-Straße 2, 85748 Garching bei München, Germany

⁵ School of Science, University of New South Wales, Australian Defence Force Academy,
Canberra, ACT 2600, Australia

⁶ INAF/Osservatorio Astrofisico di Arcetri, L.go E. Fermi 5, 50125 Firenze, Italy

Draft version November 15, 2021

ABSTRACT

Balmer-dominated shells in supernova remnants (SNRs) are produced by collisionless shocks advancing into a partially neutral medium, and are most frequently associated with Type Ia supernovae. We have analyzed Hubble Space Telescope (HST) images and VLT/MUSE or AAT/WiFeS observations of five Type Ia SNRs containing Balmer-dominated shells in the LMC: 0509–67.5, 0519–69.0, N103B, DEM L71, and 0548–70.4. Contrary to expectations, we find bright forbidden line emission from small dense knots embedded in four of these SNRs. The electron densities in some knots are higher than 10^4 cm^{-3} . The size and density of these knots are not characteristic for interstellar medium (ISM) – they most likely originate from a circumstellar medium (CSM) ejected by the SN progenitor. Physical property variations of dense knots in the SNRs appear to reflect an evolutionary effect. The recombination timescales for high densities are short, and HST images of N103B taken 3.5 yr apart already show brightness changes in some knots. VLT/MUSE observations detect [Fe XIV] line emission from reverse shocks into SN ejecta as well as forward shocks into the dense knots. Faint [O III] line emission is also detected from the Balmer shell in 0519–69.0, N103B, and DEM L71. We exclude the postshock origin because the [O III] line is narrow. For the preshock origin, we considered three possibilities: photoionization precursor, cosmic ray precursor, and neutral precursor. We conclude that the [O III] emission arises from oxygen that has been photoionized by [He II] $\lambda 304$ photons and is then collisionally excited in a shock precursor heated mainly by cosmic rays.

Subject headings: ISM: supernova remnants — Magellanic Clouds — ISM: individual (SNR 0509–67.5, SNR 0519–69.0, SNR 0509–68.7, SNR 0505–67.9, SNR 0548–70.4)

1. INTRODUCTION

Supernova remnants (SNRs) are commonly identified by diffuse X-ray emission, nonthermal radio emission, and high [S II]/H α ratio, which are characteristics produced by high-velocity shocks. However, some SNRs exhibit optical spectra that are dominated by hydrogen Balmer lines with no or very weak forbidden lines. Such “Balmer-dominated” spectra were first observed in the Tycho SNR (Kirshner & Chevalier 1978) and subsequently detected in SN 1006 (Schweizer & Lasker 1978), Kepler SNR (Fesen et al. 1989), RCW 86 (Long & Blair 1990), and Cygnus Loop (Raymond et al. 1983) in the Galaxy, and 0509–67.5, 0519–69.0, DEM L71 (0505–67.9), 0548–70.4 (Tuohy et al. 1982), and N103B (0509–68.7) (Williams et al. 2014; Li et al. 2017) in the Large Magellanic Cloud (LMC).

Of the above SNRs, only the Cygnus Loop originates from a core-collapse supernova. Its SNR shock velocities are low and [O III] and [O II] forbidden lines are seen where the shocked gas cools. The spectra of Cygnus Loop’s Balmer filaments have been modeled by a $\sim 400 \text{ km s}^{-1}$ nonradiative shock (Medina et al. 2014). The other SNRs containing Balmer-dominated shells are all of Type Ia and are young or relatively young. The weakness

or absence of forbidden lines and the observed narrow core and broad wings of their Balmer line profiles (Smith et al. 1991) can be explained by collisionless shocks advancing into a partially neutral medium (Chevalier et al. 1980). The interstellar neutral H atoms enter the shock front and can be collisionally excited and emit Balmer lines, forming the narrow core, while the postshock thermalized interstellar protons can go through charge exchange with the neutrals and emit Balmer lines, forming the broad wings (Heng 2010).

For some of the Type Ia SNRs with Balmer-dominated shells/filaments, forbidden line emission is detected at a significant level. In the cases of Kepler (Blair et al. 1991; Sankrit et al. 2008) and N103B (Li et al. 2017), bright forbidden lines are detected from dense knots that represent a circumstellar medium (CSM) ejected by the progenitor before the SN explosion, indicating that the progenitor white dwarf must have accreted material from a normal star companion.

Faint forbidden lines associated with the forward and reverse shocks in Type Ia SNRs with Balmer-dominated shells have also been reported. For example, [O I] $\lambda 6300$ line emission associated with the Balmer shell has been reported in N103B and suggested to be excited

in the cosmic ray precursors of the Balmer-dominated forward shocks (Ghavamian et al. 2017). For SNRs with a dense CSM component, such as N103B, the forward radiative or partially radiative shocks into the CSM at shock speeds of $350\text{--}450\text{ km s}^{-1}$ can excite coronal [Fe XIV] $\lambda 5303$ and other coronal lines, as seen in N103B (Ghavamian et al. 2017). Similarly, reverse shocks driven into the SN ejecta at $350\text{--}450\text{ km s}^{-1}$ speed can also excite coronal [Fe XIV] line emission, as reported in SNRs 0509–67.5, 0519–69.0, and N103B (Seitenzahl et al. 2019). In the two largest Type Ia SNRs with Balmer-dominated shells, DEM L71 and 0548–70.4, the presence of isolated patches of [O III] $\lambda 5007$ emission has been interpreted as an indication of the SNR shocks becoming radiative (Tuohy et al. 1982).

In a program to search for surviving companions of Type Ia SN progenitors in the LMC (Litke et al. 2017; Li et al. 2017, 2019), we have studied Hubble Space Telescope (HST) $H\alpha$ images of the Type Ia SNRs with Balmer-dominated shells 0509–67.5, 0519–69.0, N103B, DEM L71, and 0548–70.4, as shown in Figure 1. Unexpectedly, we find numerous nebular knots in DEM L71, similar to those seen in N103B and Kepler. We have also used archival integral field unit type observations of these five Type Ia SNRs to extract continuum-subtracted line images. These superb imaging and spectroscopic data make it possible to discover faint forbidden line emission and resolve dense knots.

This paper reports our search and analysis of forbidden line emission from five Type Ia SNRs with Balmer-dominated shells in the LMC. Section 2 describes the data used in this work, Section 3 introduces the method of our analysis, Section 4 reports results of individual SNRs, and Section 5 discusses the implication of the forbidden line emission on the nature of the SN progenitors and the SNR shocks. Section 6 summarizes this study.

2. OBSERVATIONS

2.1. Hubble Space Telescope Observations

We have obtained new HST $H\alpha$ images of SNR N103B, DEM L71, and SNR 0548–70.4, using the UVIS channel of Wide Field Camera 3 (WFC3) with the F656N filter in Program 13282 (PI: Chu). The UVIS channel of WFC3 has a $162'' \times 162''$ field of view and a $0''.04$ pixel size. The observations were dithered with the WFC3-UVIS-GAP-LINE pattern for 3 points and point spacings of $2''.414$. The total exposure time for each SNR is 1350 s.

Archival HST $H\alpha$ images of SNRs 0509–67.5 and 0519–69.0 taken with the Advanced Camera for Surveys (ACS) and the F658N filter are available in the Hubble Legacy Archive. In addition, archival HST WFC3 $H\alpha$, [O III], and [S II] images of N103B are also available.

The HST imaging observations we use are listed in Table 1, where the filter, PI, program ID, date of observation, and exposure time are given.

2.2. VLT MUSE observations

We have used archival Multi-Unit Spectroscopic Explorer (MUSE) observations obtained with the Very Large Telescope (VLT) UT4 for SNRs 0509–67.5, 0519–69.0, N103B, and DEM L71. MUSE is an integral-field unit (IFU), which provides a spectrum for every position in the field of view (FOV). For these observa-

tions, the FOV is $60'' \times 60''$, large enough to encompass the entire SNR shell for the three small objects, but not DEM L71. The wavelength coverage, $4750\text{--}9350\text{ \AA}$, includes nebular lines such as $H\alpha$, $H\beta$, [O III] $\lambda\lambda 4959, 5007$, [N II] $\lambda\lambda 6548, 6583$, and [S II] $\lambda\lambda 6716, 6731$. The spatial and spectral samplings are $0''.2\text{ spaxel}^{-1}$ and $1.25\text{ \AA pixel}^{-1}$, respectively. The archival MUSE observations are listed in Table 1 with PI, program ID, date of observation, and exposure time information.

We follow the standard procedure and use the VLT MUSE data reduction pipeline (Weilbacher et al. 2014) to carry out bias subtraction, flat fielding, and wavelength and geometrical calibrations.

2.3. ATT WiFeS observations

We have used the Wide Field Integral Spectrograph (WiFeS) observations obtained with the Advanced Technology Telescope (ATT) for SNR 0548–70.4.

The FOV of ATT WiFeS is $25'' \times 38''$, much smaller than the extent of SNR 0548–70.4. Thus, observations for a grid of 3×5 fields were planned to map the entire SNR, as shown in Figure 2; however, due to the weather condition, only four fields were observed. Among these observed fields, only fields G4 and G9 have adequate quality and contain forbidden line emission to be presented in this study.

The ATT WiFeS is a double-beam spectrograph that simultaneously covers the blue and red wavelength ranges. For SNR 0548–70.4, the B3000 and R7000 gratings were used for the blue ($3500\text{--}5700\text{ \AA}$), and the red ($5400\text{--}7024\text{ \AA}$) wavelength ranges, respectively. The overall wavelength coverage is thus $3500\text{--}7024\text{ \AA}$, which includes all major nebular lines in the optical. The spatial sampling is $1''.0 \times 0''.5\text{ spaxel}^{-1}$, while the spectral samplings are $0.768\text{ \AA pixel}^{-1}$ for the blue spectral range and $0.439\text{ \AA pixel}^{-1}$ for the red spectral range. The ATT WiFeS observation of SNR 0548–70.4 is listed in Table 1 with pertinent information, such as PI, program ID, date of observation, and exposure time.

3. METHOD OF ANALYSIS

We start our analysis with a general examination of the HST $H\alpha$ images of the five Type Ia SNRs with Balmer-dominated shells in the LMC. HST images allow us to resolve nebular features as small as $0''.05$, i.e., 0.0125 pc in the LMC. We have learned from our previous study of the SNR N103B that HST $H\alpha$ images resolve two major types of morphological features: Balmer-dominated long filaments that delineate a shell structure, and forbidden-line-emitting dense knots that are distributed in groups in the SNR interior or along some Balmer filaments (Li et al. 2017). Thus, we first use the HST $H\alpha$ images to examine the shell structure and to search for dense nebular knots.

We then extract nebular line images from the VLT MUSE and ATT WiFeS data to search for nebular features that emit forbidden lines. These IFU data cubes allow us to extract images in wavelength intervals that cover nebular lines as well as images in adjacent line-free wavelength intervals. A clean line image can be obtained by subtracting the latter from the former. So-extracted line images are more sensitive than ground-based images

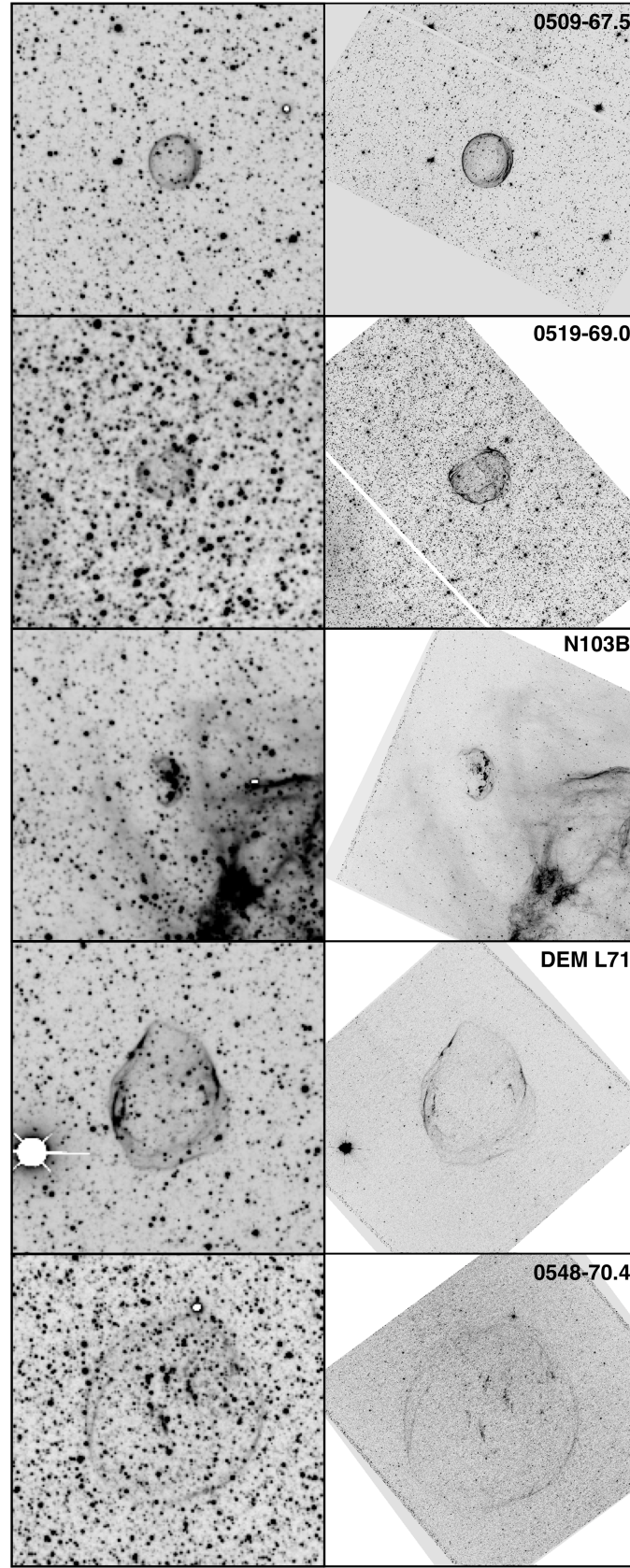


FIG. 1.— $H\alpha$ images of the five LMC Type Ia SNRs with Balmer-dominated shells: 0509–67.5, 0519–69.0, N103B, DEM L71, and 0548–70.4 (from top to bottom). Images in the left panels were obtained with the MOSAIC II camera on the Blanco 4 m Telescope at Cerro Tololo Inter-American Observatory, and images in the right panels were taken with the Hubble Space Telescope. The field of view of each panel is $3' \times 3'$ with North at the top and East to the left.

TABLE 1
OBSERVATIONS

Telescope	Instrument	SNR	Filter	PI	Program ID	Date	t_{exp} (s)
HST	ACS/WFC	0509–67.5	F658N	Hughes	11015	2006 Oct 28	4620
HST	WFPC2	0509–67.5	F656N	Hughes	11015	2007 Nov 07	14300
HST	ACS/WFC	0509–67.5	F658N	Hovey	14733	2016 Nov 13	10662
HST	ACS/WFC	0519–69.0	F658N	Hughes	12017	2011 Apr 21	4757
HST	WFC3/UVIS	N103B	F656N	Chu	13282	2013 Jul 11	1350
HST	WFC3/UVIS	N103B	F502N	Williams	14359	2017 Jan 03	2051
HST	WFC3/UVIS	N103B	F657N	Williams	14359	2017 Jan 03	2979
HST	WFC3/UVIS	N103B	F673N	Williams	14359	2017 Jan 03	1982
HST	WFC3/UVIS	DEM L 71	F656N	Chu	13282	2014 Mar 05	1350
HST	WFC3/UVIS	0548–70.4	F656N	Chu	13282	2013 Sep 20	1350
VLT	MUSE	0509–67.5	-	Morlino	0100.D-0151	2018 Jan 22	701
VLT	MUSE	0519–69.0	-	Leibundgut	096.D-0352	2016 Jan 17	900
VLT	MUSE	N103B	-	Leibundgut	096.D-0352	2015 Dec 12	900
VLT	MUSE	DEM L71	-	Leibundgut	096.D-0352	2015 Nov 16	900
ATT	WiFeS	0548–70.4	-	Seitenzahl	4150178	2015 Dec 14	1800

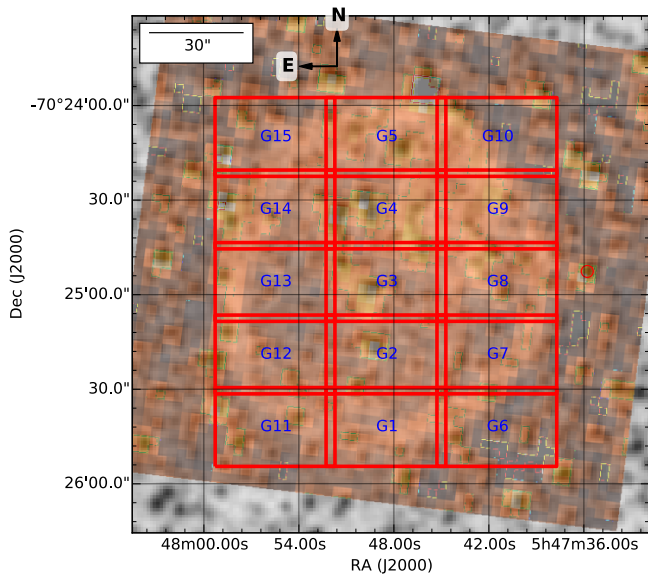


FIG. 2.— ATT WiFeS $H\alpha$ observations of 0548–70.4. Only G4 and G9 data with better quality are presented in this paper.

taken with filters because sky lines and continuum background, especially the stars, are both removed. It is thus not surprising that we indeed have detected faint emission features that were not seen before.

A large number of forbidden lines of low-ionization species, such as [N II], [O I], [O III], [S II], [Ca II], and [Ni II], are detected in the dense knots (Ghavamian et al. 2017; Dopita et al. 2019), and forbidden lines of high-ionization species, such as [Fe IX], [Fe XIV], [Fe XV], and [S XII], are detected in nonradiative shocked ejecta (Seitzzahl et al. 2019); however, we will focus on only the strongest diagnostic lines in this paper. The line images extracted include those of $H\alpha$, [O III] $\lambda 5007$, [Fe XIV] $\lambda 5303$, [O I] $\lambda 6300$, and [S II] $\lambda\lambda 6716, 6731$ lines. The central wavelengths are these nebular lines red-shifted to the LMC velocity of $\sim 270 \text{ km s}^{-1}$. A wavelength interval of 10 \AA is used for the $H\alpha$ line image (corresponding to $\pm 230 \text{ km s}^{-1}$) to avoid the [N II] lines, 8 \AA for [O III] (corresponding to $\pm 240 \text{ km s}^{-1}$) to accommodate emission at all velocities, 20 or 150 \AA for [Fe XIV] (corresponding to ± 570 and $\pm 4250 \text{ km s}^{-1}$, respectively) to accommodate its broad line profile, 15 \AA for [O I] (corresponding to $\pm 360 \text{ km s}^{-1}$), and 31 \AA for [S II] to include both $\lambda\lambda 6716, 6731$ lines. For the line-free continuum background images, wavelength intervals of 12 – 25 \AA are used on the two sides of each spectral line interval. The average of the two spectral-background images is prorated and subtracted from the line image to obtain spectral-background-subtracted clean line image. Throughout the rest of the paper, only such clean line images are used and we will refer to them simply as “line image”.

As these line images have the same FOV and image scale, they can be inter-compared directly to search for forbidden-line emission features. These $H\alpha$ images can be compared with the HST $H\alpha$ images for detailed physical structures of emission features. We note that some

stars have negative values in the MUSE $H\alpha$ line images because their spectra have the $H\alpha$ line in absorption.

Finally, we analyze the spectral properties of the forbidden-line emission features, measuring their line strengths relative to Balmer lines and using the [N II] $\lambda 5755/\lambda 6583$ diagnostic to determine electron temperatures and the [S II] $\lambda 6716/\lambda 6731$ diagnostic to determine electron densities. These physical parameters are used to assess the physical conditions of the forbidden-line emission features in order to determine their origin.

4. RESULTS OF INDIVIDUAL OBJECTS

The five Type Ia SNRs with Balmer-dominated shells we have studied are shown in Figure 1, where the same image scale is used for all five SNRs for easier inter-comparison. The results of our analyses of these five SNRs are described below. See the Appendix for representative spectra of different morphological features in the SNR and of the background ISM, plotted in two wavelength ranges that cover the $H\beta + [\text{O III}]$ lines and $H\alpha + [\text{N II}] + [\text{S II}]$ lines, respectively.

4.1. SNR 0509–67.5 (Figure 3)

The HST $H\alpha$ image of SNR 0509–67.5 exhibits an overall regular and slightly elliptical shell, as shown in Figure 3a. The eastern side of the shell shows one major filament delineating the rim, indicating a simple shell structure, while the western side exhibits multiple filaments along the rim that has been suggested to be caused by a non-uniform ambient medium (Hovey et al. 2015). The bright filaments originate from locations where the sight line is tangent to the shock front, while the diffuse emission near or between the filaments originates from locations where the shock front is oblique to the line of sight. No dense $H\alpha$ knots are seen in SNR 0509–67.5.

The MUSE $H\alpha$ image of SNR 0509–67.5 detects not only the shell rim but also diffuse emission throughout the face of the SNR, including the central region where the SNR shocks propagate along the lines of sight and the emitting path lengths are the shortest. This image also detects a faint $H\alpha$ halo just outside the SNR shell. This halo, not detected in the HST $H\alpha$ image, most likely originates from the ambient medium photoionized by the UV precursor of the SNR shocks. Beyond the halo, to the east and southeast of the SNR exist three broad streamer-like features that are most likely from the interstellar background and are better seen in the [S II] image.

The MUSE [O III] line image shows some diffuse emission from the ISM background, but no [O III] emission from the Balmer shell or the halo around the shell. Note that the MUSE spectra show an emission line near $\lambda 5019$ – 5022 \AA , but this line corresponds to the Doppler shifted He I $\lambda 5015$ line.

The MUSE [Fe XIV] line image shows the reverse shock front into the SN ejecta. As illustrated in the color composite of $H\alpha$, X-ray, and [Fe XIV] images in Figure 1 of Seitzzahl et al. (2019), the $H\alpha$ emission from the forward collisionless shock is located at the largest radius, the [Fe XIV] emission behind the reverse shock is located at the smallest radius, while the X-ray emission is sandwiched between these two shock fronts.

The MUSE [S II] line image shows a completely different picture from the $H\alpha$ line image. Neither the filamen-

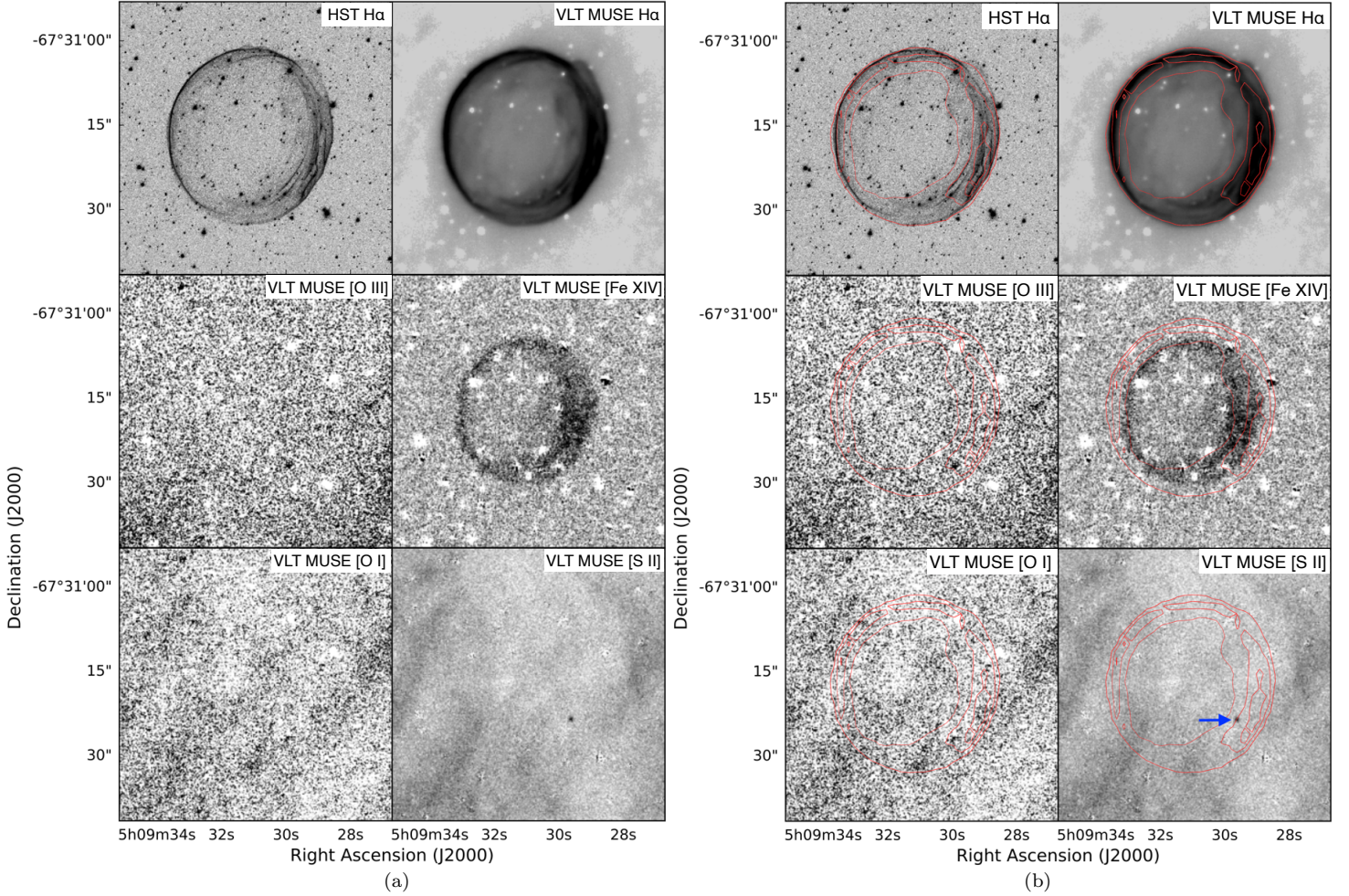


FIG. 3.— (a): HST $H\alpha$ and VLT MUSE $H\alpha$, [O III], [Fe XIV], [O I], and [S II] images of SNR 0509–67.5. (b): Same as panel (a), but with VLT MUSE $H\alpha$ contours overplotted. In the [S II] image, an blue arrow points to a galaxy that is a residue from the spectral background subtraction.

tary Balmer shell nor the faint diffuse $H\alpha$ halo is detected in [S II]. The most prominent [S II] emission appears in diffuse arcs and streamer-like features on scales larger than the SNR. The streamer-like features to the east of the SNR have counterparts in the MUSE $H\alpha$ and [O I] line images. The irregular distribution of these [S II] features suggests that they originate from a background ISM.

The MUSE [O I] line image shows essentially the same kind of diffuse arcs and streamer-like features that are seen in the [S II] image. No [O I] emission can be unambiguously associated with the SNR per se.

The [S II] line strength relative to the respective nearest Balmer lines for the SNR and the interstellar background are given in Table 2. To determine the forbidden line strengths at the Balmer shell rim, it is necessary to subtract the background. In the [S II] lines, the background is not only bright but also nonuniform. The [S II]/ $H\alpha$ ratio of the filamentary Balmer shell reported in Table 2 is derived by using a medium to low background value. If a higher background value is used, the [S II]/ $H\alpha$ becomes negative. The “:” symbol denotes a non-detection, and the error is dominated by the uncertainties in the background subtraction. The faint Balmer

halo is not detected in [O III] or [S II], and the large variations in the background ISM emission make it impossible to make meaningful estimates of their upper limits. The [S II]/ $H\alpha$ ratio of the background ISM exhibits a range of values, as given in Table 2. The [S II] $\lambda 6716/\lambda 6731$ line ratio of the background is in the low-density limit, <100 H-atom cm^{-3} , consistent with an ISM origin.

Note that the emission “knot” in the southwest quadrant of the SNR in the MUSE [S II] image, marked by an arrow in Figure 3b, originates from two emission lines at $\lambda 6729$ and $\lambda 6734$. These two lines cannot be the [S II] doublet from 0509–67.5 in the LMC. Instead, these emission lines must be the [O II] $\lambda\lambda 3726, 3729$ lines from a background galaxy at $z = 0.806$, similar to the background galaxy near the center of 0509–67.5 (Litke et al. 2017). The ratio of the red-shifted [O II] doublet indicates a density near 100 H cm^{-3} , consistent with densities of an ISM.

4.2. SNR 0519–69.0 (Figure 4)

The HST $H\alpha$ image of SNR 0519–69.0 shows a more complex morphology than that of 0509–67.5. The SNR shell rim from east through south and west to the north is roughly round, with morphological features suggestive

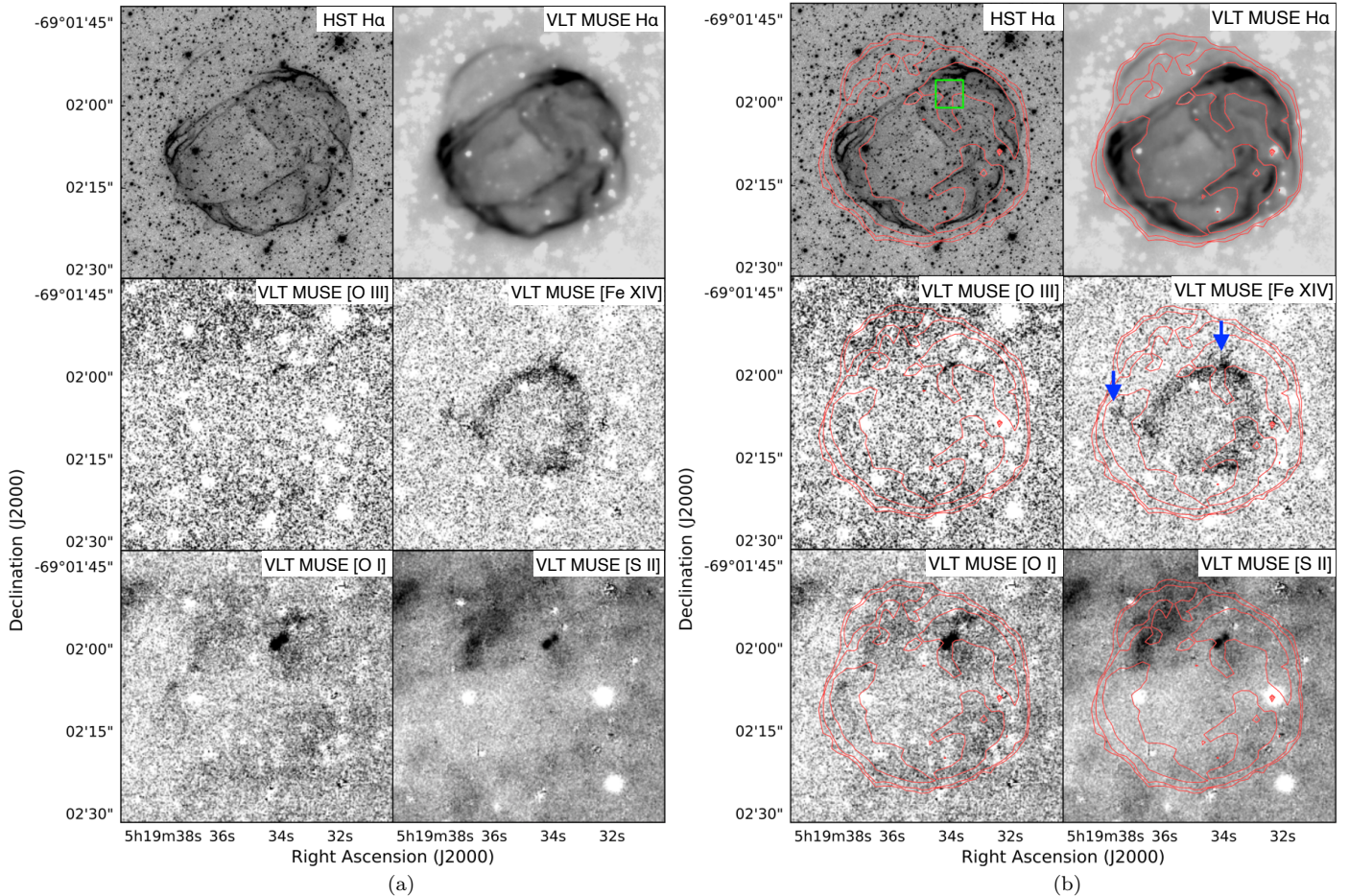


FIG. 4.— Same as Figure 3, but for SNR 0519–69.0. The green square marks the region shown in Figure 8, which illustrates the morphology of knots. See Section 5.1.1. The blue arrows mark two additional patches of [Fe XIV] emission.

of a “bubbly” shell surface. The northeastern quadrant of the SNR shell rim appears flattened; however, in this direction a faint filamentary arc is detected at larger distances than the average shell radius in the other quadrants. It is likely that the faint outer arc represents the shock front in the northeastern quadrant, while the bright flattened filament and the bright interior semi-straight filament in the southwestern quadrant may have formed by the same mechanism. No dense knots similar to those in N103B are seen in this $H\alpha$ image of SNR 0519–69.0.

SNR 0519–69.0’s MUSE $H\alpha$ line image shows a qualitatively similar morphology at a lower resolution than its HST $H\alpha$ image (see Figure 4). The MUSE $H\alpha$ image detects emission over the face of the SNR and slightly beyond the SNR radius, similar to what is seen in 0509–67.5, although the diffuse $H\alpha$ halo of 0519–69.0 is not as extended. This diffuse $H\alpha$ halo is marginally detected in the HST $H\alpha$ image. Similarly, this halo most likely originates from an ambient medium photoionized by the SNR shock’s UV precursor, as in the case of 0509–67.5. Beyond the halo, SNR 0519–69.0 is surrounded by diffuse, patchy $H\alpha$ emission associated with ambient or background ISM.

The MUSE [O III] line image reveal a small patch of emission in the SNR interior, and this patch is much more

prominent in the [S II] and [O I] lines images, as shown later in this section. This [O III] image also shows a very weak partial counterpart of the Balmer shell: detected from the east through the south to the southwest along the bright rim and possibly along the faint outer rim in the southwest quadrant. We have carefully separated the [O III] line emission from the He I $\lambda 5015$ line emission; however, the faint high-velocity wings may overlap and contribute to low-level contamination in limited regions where both lines are detected. No [O III] counterpart of the faint $H\alpha$ halo is detected. [O III] emission from the diffuse background ISM is detected to the north and to the south of the SNR.

The [Fe XIV] line image shows a shell associated with the reverse shock front into the SN ejecta, similar to that seen in SNR 0609–67.5. However, 0619–69.0 shows two additional patches of [Fe XIV] emission, marked by arrows in Figure 4b. The east patch is projected near the brightest part of the Balmer shell’s eastern rim, while the north patch is projected near the one o’clock position of the [Fe XIV] ring. These two small patches have a different origin from the [Fe XIV] shell associated with the reverse shock, as the FWHM of the line profile is $\sim 300 \text{ km s}^{-1}$ in the patches and a few $\times 10^3 \text{ km s}^{-1}$ in the shell. The north patch emits brightly in [O I] and [S II] and faintly in [O III]; the east patch shows [O III]

and [O I] emission, but it is difficult to disentangle the contributions from the Balmer shell and the east patch.

The [S II] line image reveals two distinct knots of bright emission projected within the SNR shell, about half way from the shell center to the bright $H\alpha$ shell rim in the north. These [S II] knots are coincident with the north patch of [Fe XIV] emission, and have faint counterparts in the [O III] line image, too. In the MUSE $H\alpha$ image, these knots blend in with Balmer filaments and do not appear as distinct features; however, the HST $H\alpha$ image reveals that the two knots are connected by diffuse emission of lower surface brightness and the knots have diameters of $\lesssim 0''.3$ (0.075 pc). These nebular knots are so small that they easily escape detection if the HST $H\alpha$ image alone is examined. The presence of these isolated small knots is very intriguing and their origin will be discussed later in this paper. Besides these knots, no [S II] emission can be unambiguously associated with the Balmer shell or the faint $H\alpha$ halo, although an irregular diffuse ISM emission background is clearly detected.

The [O I] line image shows not only bright counterpart of the north [Fe XIV] patch that is coincident with the [S II] knots, but also enhanced emission at the east [Fe XIV] patch that is not detected in [S II]. In addition, [O I] emission is seen along the southern half of the Balmer shell rim. There is enhanced [O I] emission enclosed within the northern part of the Balmer shell, but it is not clear whether the [O I] emission is associated with the SNR shell or the background diffuse ISM.

The [O III] and [S II] line emission from the Balmer shell and the background ISM of 0519–69.0 is measured in a similar fashion as that of 0509–67.5. The two dense knots in 0519–69.0 are measured with very high signal-to-noise ratios. The [S II]/ $H\alpha$ and [O III]/ $H\beta$ ratios of the Balmer shell, dense knots, and the background ISM are given in Table 2. The [S II] doublet ratio of the background is in the low density limit and consistent with an ISM origin.

4.3. SNR N103B (Figure 5)

The HST $H\alpha$ image of SNR N103B clearly reveals a filamentary shell structure that encompasses prominent groups of dense knots. Only the filamentary shell is Balmer-dominated, and the dense knots represent a CSM ejected by the SN progenitor (Williams et al. 2014; Li et al. 2017). The shell is elliptical with an opening to the east. The knots are mainly distributed in four groups, with only few knots located along $H\alpha$ filaments near the shell rim. Almost all knots are seen on the western side of the shell interior. The knots individually can have sizes as small as $0''.14$ (0.035 pc) in diameter, while a group of knots can be as extended as $2''$ (0.5 pc) across.

N103B’s MUSE $H\alpha$ line image shows bright nebular knots in the interior of an incomplete shell, similar to those seen in the HST $H\alpha$ image, except the “knots” seen in the MUSE image correspond to “groups of knots” in the HST image. The MUSE $H\alpha$ image also shows that N103B is projected in a complex diffuse background with multiple filaments and arcs in the surroundings.

The MUSE [O III] line image shows bright emission from the knots, and very faint emission from the Balmer-dominated shell. The surrounding ionized ISM is also detected in the [O III] image with a surface brightness distribution following that of the $H\alpha$ image roughly but

not exactly. The [O III]/ $H\alpha$ ratio varies among the CSM knots and in the surrounding ISM; their values are given in Table 2.

The MUSE [Fe XIV] line image shows bright emission from the CSM knots and an arc extending to the east. This arc has no counterpart in other optical line images; however, it follows an X-ray arc closely (Seitenzahl et al. 2019). The FWHM of the [Fe XIV] line profile is up to 3300 km s^{-1} in the arc, and 400 km s^{-1} in the knots. These widths and spatial distributions are consistent with the origin of reverse shock into the SN ejecta for the arc, and forward shock into the CSM for the knots.

The MUSE [S II] line image shows bright emission from the knots, but no emission from the Balmer-dominated shell. The [S II] emission from the surrounding ISM follows $H\alpha$ emission well. The [S II] image also shows two intriguing concentric ring-like structures: the inner ring has a radius of 4.9 pc and roughly encompasses the SNR, while the outer ring is 5.9 pc in size and is projected in a background with low $H\alpha$ surface brightness.

The MUSE [O I] image shows bright emission from the CSM knots. The background emission from diffuse ISM is also detected at a much lower level than the CSM knots.

In summary, N103B has prominent forbidden line emission from the CSM knots, faint [O III] line emission from the Balmer-dominated shell, and moderately bright forbidden line emission from the surrounding ISM. The representative ranges of forbidden line strengths from different features in and around the SNR N103B are given in Table 2. The dense knots’ electron densities determined from the [S II] doublet are 10^3 – 10^4 cm^{-3} , consistent with the 3×10^4 – 10^5 cm^{-3} determined from the UV lines of Si III (Blair et al. 2020), and their electron temperatures determined from the [N II] $\lambda 6583$ and $\lambda 5577$ lines are 10,000 – 20,000 K. The electron density of the background is below 100 cm^{-3} , consistent with an ISM origin.

4.4. SNR DEM L71 (Figure 6)

The HST $H\alpha$ image shows that DEM L71’s SNR shell is quite irregular. The eastern and southwestern sides of the shell contain interior filaments curved along the outer rim. The northern and southwestern parts of the shell rim bulge out, suggestive of blow-outs into a lower-density medium. Upon closer inspection, small knots can be seen distributed along some interior filaments and outer rim. The smallest nebular knots have diameters $\lesssim 0''.3$ (0.075 pc). A small number of nebular knots are projected in the shell interior, and they appear diffuse with lower surface brightness.

DEM L71’s MUSE $H\alpha$ line image has a smaller field of view than the HST $H\alpha$ image. In the MUSE $H\alpha$ image, the eastern part of the main SNR shell is clearly detected but the shell rims in the other directions are outside the field of view. The MUSE $H\alpha$ image, being much deeper than the HST $H\alpha$ image, reveals numerous filaments within the SNR shell, especially those curved along the shell rim from the east through the south to the west. In addition, some $H\alpha$ nebular knots are detected.

The MUSE [O III] line image shows a very different morphology: bright knots are detected along the aforementioned curved filaments interior to the shell, and some knots are projected in the central cavity without

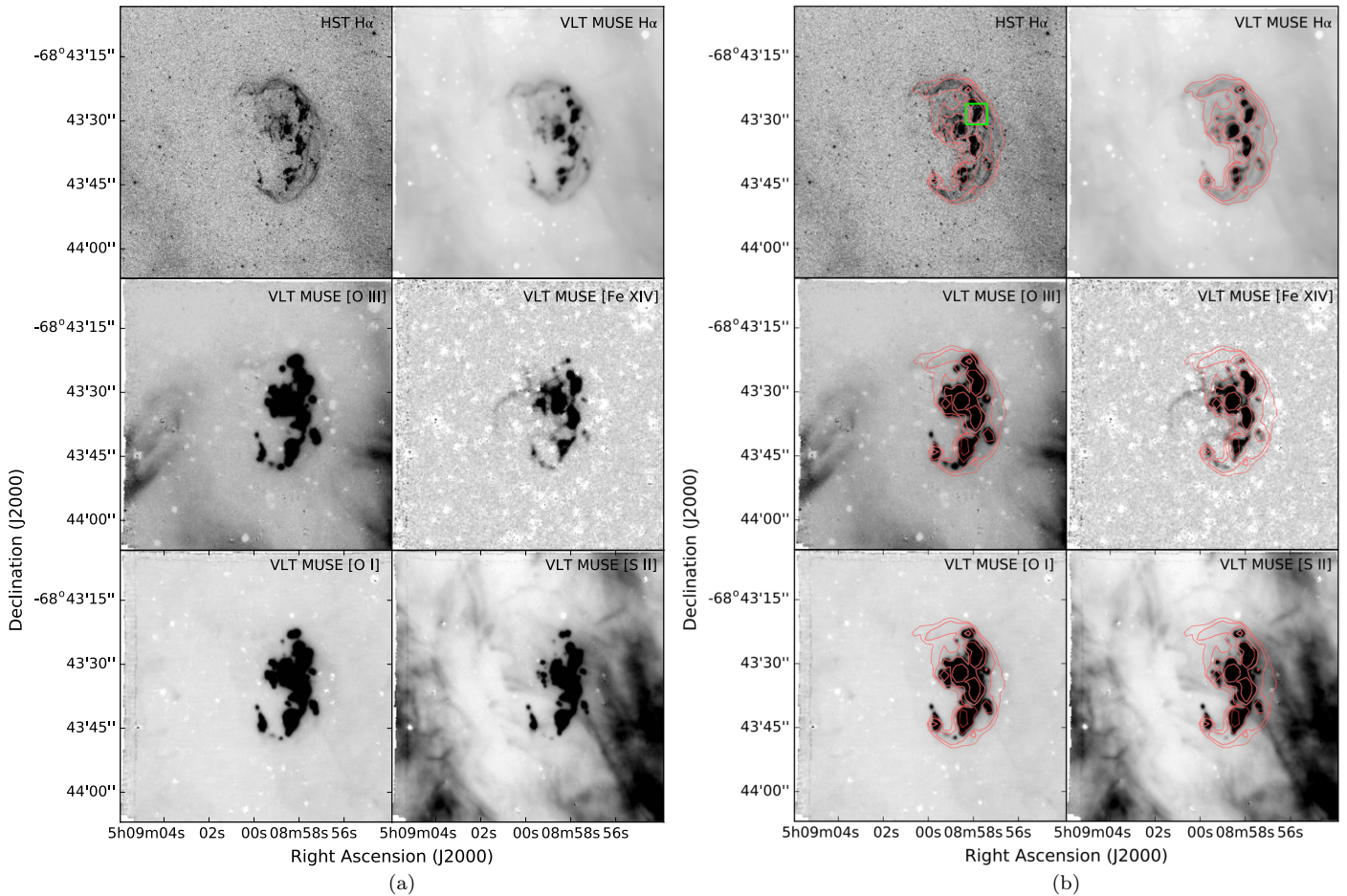


FIG. 5.— Same as Figure 4, but for SNR N103B.

association with filaments. The [O III] image also detects faint counterpart of the eastern rim of the Balmer-dominated shell. Also detected is a band of diffuse emission extending from the top center southwestwards to the bottom of the field of view.

The MUSE [Fe XIV] line image shows emission from the knots near the east rim and northwest rim. In addition, [Fe XIV] emission is detected along the Balmer shell rim on the east and west sides of the SNR. It is interesting that the [Fe XIV] arcs follow X-ray emission that delineates the forward shocks into the ISM. This is quite different from what we see in 0509–67.5, 0519–9.0, and N103B.

The MUSE [S II] line image shows nebular knots even more prominently than the [O III] image, detecting more faint knots. The MUSE [S II] image also detects faint emission from the Balmer-dominated shell rim on the east. The [S II] image of DEM L71 has also detected the northern part of the band of diffuse emission seen in the [O III] image.

The MUSE [O I] line image shows emission from both knots and the Balmer shell rim on the east side. The [O I] image is qualitatively similar to the [S II] image, although the [O I] emission along the Balmer shell rim is more prominent.

The MUSE observation of DEM L71 covered only a small area of sky outside the SNR shell. While this sky

coverage is adequate for background subtraction from bright features of small sizes, such as the Balmer shell rim and knots, it is inadequate for accurate measurements of forbidden line emission from the background per se or background subtraction for extended features, such as the band of diffuse emission across the face of DEM L71. Therefore, only the Balmer shell and the knots are reported in Table 2. The electron densities of the knots are in the range from 650 to over $10,000 \text{ cm}^{-3}$, and the electron temperatures are $\sim 13,000 \text{ K}$. The electron density derived from the [S II] doublet of the SNR shell rim is in the low-density limit, $< 100 \text{ cm}^{-3}$.

4.5. SNR 0548–70.4 (Figures 7a and 7b)

The HST H α image of SNR 0548–70.4 has the lowest signal-to-noise ratio compared to similar observations of N103B and DEM L71, because of the relatively low surface brightness of 0548–70.4. The Balmer-dominated shell of 0548–70.4 appears quite regular (see Figure 1), although it shows double-rim morphology along the northeastern quadrant, similar to those seen in DEM L71. Projected near the central region of 0548–70.4 are four strips of diffuse emission with some of them containing nebular “rods” that are $0''.25$ (0.063 pc) in width and up to $2''$ (0.5 pc) in length. There is also enhanced nebular emission, possibly similar to knots or rods, along a filament near the northwestern rim.

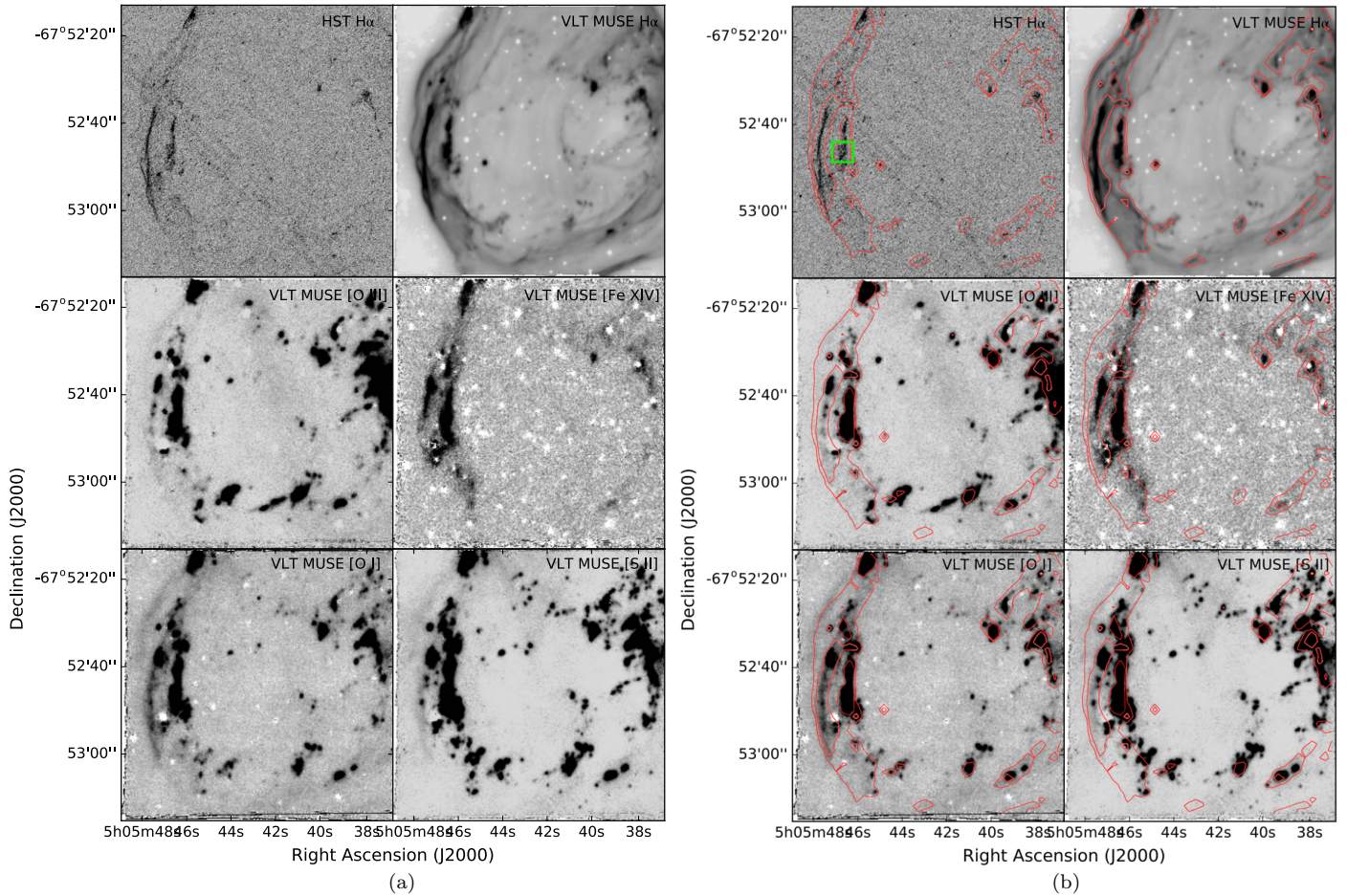


FIG. 6.— Same as Figure 4, but for SNR DEM L71.

The ATT WiFeS observations of SNR 0548–70.4 mapped the entire remnant (Fig. 2); however, only data of the G4 and G9 fields are of adequate quality to extract spectral information. The G9 field includes a segment of the Balmer-dominated shell rim and one of the four aforementioned strips of diffuse emission in the central region of the SNR (Fig. 7a). The [O III], [O I], and [S II] line images detect emission from knots and the strip of diffuse emission, but the Balmer-dominated shell rim is not unambiguously detected in any of the forbidden line images. The [Fe XIV] line is not detected anywhere. The G4 field includes strips of diffuse emission with embedded knots (Fig. 7b). These features are detected in [O III], [O I], and [S II] line images. The [Fe XIV] line is not detected. The relative strengths of the [O III], [O I], and [S II] lines vary among the emission regions. The ranges of representative [O III]/H β and [S II]/H α ratios are given in Table 2.

5. DISCUSSION

We have found three sources of forbidden line emission in Type Ia SNRs with Balmer-Dominated Shells: bright emission from dense knots inside the SNRs, [Fe XIV] emission from reverse shocks into the SN ejecta, and faint emission associated with the collisionless shocks. The physical properties and origins of these sources are discussed below.

5.1. Dense Knots

5.1.1. Physical Properties of the Knots

The content and distribution of dense knots are different among the five Type Ia SNRs with Balmer-Dominated Shells we studied: in ground-based [S II] images, 0509–67.5 has no knots at all, 0519–69.0 has two knots close together in the northwest quadrant of the SNR, N103B has prominent groups of knots distributed only in the west side of the SNR, DEM L71 has bright knots distributed along inner Balmer filaments in a ring-like structure with fainter knots projected interior to the ring, and 0548–70.4 has knots distributed mostly within a few patches projected near the central region of the SNR.

The “knots” detected in ground-based images are often resolved into multiple smaller knots in HST images. The morphologies of these small knots are different among the SNRs. HST H α images show that some knots are round or slightly elongated with minor axis as small as $\sim 0''.2$ and major-to-minor axis ratio ranging from 1.0 to a few, as seen in N103B and DEM L71, while some knots are rod-like with widths of $\sim 0''.2$ and lengths of $2''$ – $3''$, as seen in 0548–70.4. The knots in 0519–69.0 are best detected in the MUSE [O I] and [S II] line images where two knots are seen. The HST H α image resolved these knots into knots as small as $0''.3$ (0.075 pc) in diameter

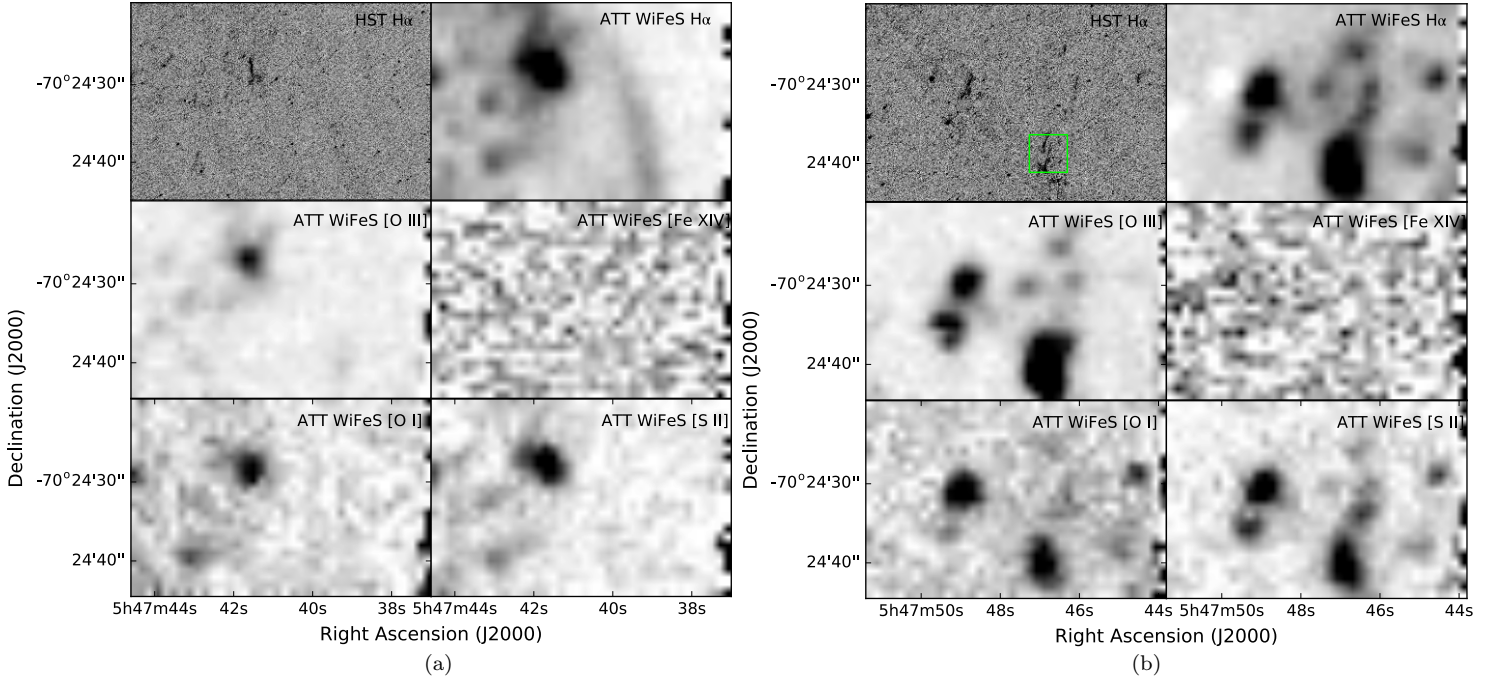


FIG. 7.— (a): HST H α and ATT WiFeS H α , [O III], [Fe XIV], [O I], and [S II] images for the G9 data of SNR 0548–70.4. (b): Same as panel (a), but for the G4 data of SNR 0548–70.4. The green square marks the region shown in Figure 8, which illustrates the morphology of knots.

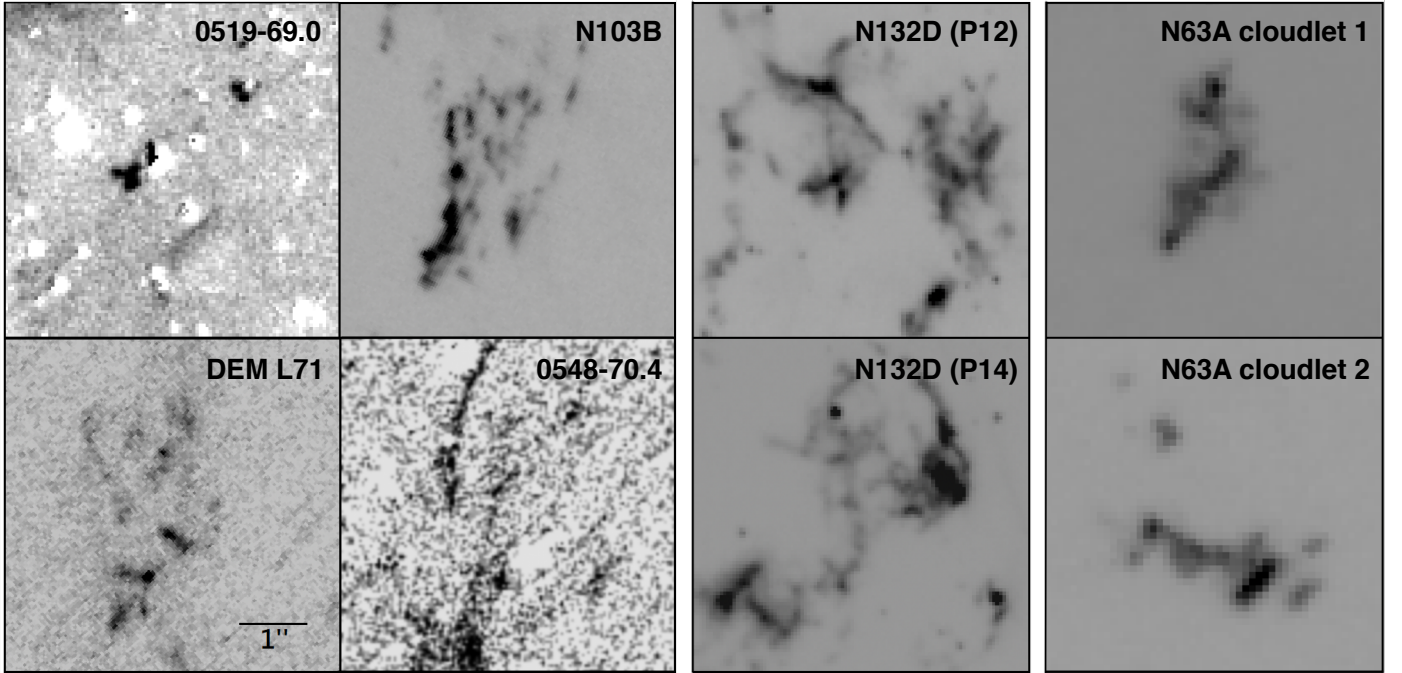


FIG. 8.— The HST H α images showing different morphologies of knots in four SNRs 0519–69.0, N103B, DEM L71, 0548–70.4. The continuum emission has been subtracted from the 0519–69.0 and 0548–70.4 H α images. The field of view of each panel is $5''0 \times 5''0$. These regions are marked with green squares in Figures 4b, 5b, 6b, and 7b. The P12 and P14 regions of SNR N132D in Dopita et al. (2018) and cloudlets of N63A in Chu et al. (1999) are also shown for comparisons.

TABLE 2
 REPRESENTATIVE PHYSICAL QUANTITIES AND PROPERTIES IN AND AROUND SNRS WITH BALMER-DOMINATED SHELLS

SNR ^a	Age (yr)	Features	[S II]/H α	[O III]/H β	n _e (cm ⁻³)	T (K)
0509–67.5	400±50 ^b	Filamentary Shell	< 0.004 ± 0.032:
...	...	Background ISM	(0.9 – 1.5) ± 0.1	...	< 100	...
...	...	Filamentary Shell	< 0.026 ± 0.041:	≤ 0.017 ± 0.003
0519–69.0	600±200 ^b	Bright Knots	(0.2 – 1.0) ± 0.0	(0.2 – 1.5) ± 0.2	1,500 – ≥10,000	...
...	...	Background ISM	(0.5 – 0.9) ± 0.2	(0.0 – 0.8) ± 0.1	< 100	...
...	...	Filamentary Shell	< 0.062 ± 0.130:	≤ 0.093 ± 0.011
N103B	860 ^b	Bright Knots	(0.1 – 0.6) ± 0.0	(0.2 – 2.6) ± 0.0	1,000 – ≥10,000	9,000 – 19,000
...	...	Background ISM	(0.1 – 0.5) ± 0.1	(0.1 – 0.9) ± 0.1	< 100	...
...	...	Filamentary Shell	< 0.034 ± 0.016	≤ 0.043 ± 0.005	< 100	...
DEML71	4,360±290 ^c	Bright Knots	(0.2 – 1.3) ± 0.0	(0.2 – 5.5) ± 0.0	650 – ≥10,000	11,000 ^d
...	...	Background ISM
...	...	Filamentary Shell	< 0.03 ± 0.01:	≤ 1.15 ± 0.13
0548–70.4	~10,000 ^e	Bright Knots	(0.3 – 0.7) ± 0.0	(1.9 – 5.6) ± 0.4	400 – 2,500	...
...	...	Background ISM	(0.1 – 0.5) ± 0.1	(2.1 – 2.6) ± 0.6	< 100	...

^a Integrated H α fluxes measured from the MUSE data are: 1.5×10^{-13} , 2.9×10^{-13} , 1.2×10^{-12} , and $> 6.7 \times 10^{-13}$ erg s⁻¹ cm⁻² for 0509–67.5, 0519–69.0, N103B, and DEML71, respectively. Note that the MUSE field is too small to cover the entire DEML71 and the H α flux of DEML71 represents only a lower limit.

^b From Rest et al. (2005).

^c From Ghavamian et al. (2003).

^d Very few knots have [N II] λ 5755 line clearly detected.

^e From Hendrick et al. (2003).

and connecting filaments. The different morphologies of knots are illustrated in Figure 8.

The spectral properties vary among the knots as well. The variations can be easily seen from comparisons among the line images. For example, N103B and DEM L71 have knots that are well detected in [O III] but appear very faint in [S II], and vice versa. Most interestingly, of the two [Fe XIV] knots in 0519–69.0 (marked in Figure 4, one is bright in [S II] and [O I] but faint in [O III], while the other has faint counterparts in [O I] and [O III] but not detected in [S II].

Electron densities of the knots, determined from the [S II] $\lambda 6716/\lambda 6731$ ratios, range from a few $\times 10^2$ to 10^4 cm^{-3} . 0548–70.4 has the lowest density in the knots, which also have the rod-like morphology.

The [O III]/H β ratios of the knots range from 0.2 to 5.6: 0519–69.0 and N103B have lower values in general, and DEM L71 and 0548–70.4 extend to higher values (see Figure 9). The [S II]/H α ratios of the knots range from 0.1 to 1.3. The low values of [S II]/H α ratio are associated with the densest knots whose high densities, $\geq 10^4$ cm^{-3} , exceed the critical densities of the [S II] $\lambda\lambda 6716, 6731$ lines, as seen in Figure 10 and elaborated later in Section 5.1.2.

The [N II] $\lambda 5755/\lambda 6584$ ratios can be used to diagnose electron temperatures. The weak [N II] $\lambda 5755$ line is detected only in knots of N103B and DEM L71. N103B has a large number of bright knots and their electron temperatures range from 9,000 to 19,000 K. In DEM L71 only the very few brightest knots are detected in the [N II] $\lambda 5755$ line and their temperatures are $\sim 11,000$ K.

5.1.2. Origin and Implication of the Knots

The knots resolved in HST H α images of these five Type Ia SNRs are small, dense, and H-rich. The size, as small as 0.05 pc, and density, as high as $\geq 10,000$ H cm^{-3} , are not characteristic for the ISM. In the HST program 13282, H α images of four larger and more evolved Type Ia SNRs are available – 0454–67.2, DEM L238, DEM L249, and DEM L316A. None of these Type Ia SNRs show small dense knots in their interiors or along their shell rims. The HST archive has H α and/or [O III] images of six core-collapse SNRs in the LMC – N49, N63A, and N206 from program 8110, 0540–69.3 from programs 6120 and 7340, and N132D from program 12001, and SN1987A from multiple programs. Among these, only N63A and N132D have small features that can be compared with the knots seen in the 5 Type Ia SNRs we have studied. Figure 8 shows that the cloudlets in N63A and N132D are qualitatively similar to the knots in the Type Ia SNRs, and they are known to be interacting with molecular clouds (Sano et al. 2019, 2020). However, the rms electron densities in the cloudlets in N63A are 150–700 cm^{-3} (Chu et al. 1999) and the electron densities of the knots in N132D are generally 2000–4000 cm^{-3} (Dopita et al. 2018), much lower than what we see in the knots in Type Ia SNRs with Balmer-Dominated Shells. SN1987A is transitioning from a SN to an SNR, and only the knots in its inner ring have sizes ~ 0.03 pc and densities 1,000–30,000 atoms cm^{-3} (Mattila et al. 2010), comparable to the knots we see in Type Ia SNRs. The rings around SN1987A are known to be of a CSM origin. We thus consider that the small knots observed in the Type Ia SNRs with Balmer-Dominated Shells most

likely belong to a CSM.

The dense knots in 0519–69.0 are not as numerous and wide-spread as those in N103B, DEM L71, and 0548–70.4. The brightest ones are concentrated in a small $0''.5 \times 3''$ (0.13 pc \times 3 pc) patch, coincident with the north patch of [Fe XIV] emission. The east patch of [Fe XIV] emission may also be associated with dense knots; however, it is superposed on a very bright Balmer shell rim and its counterparts in [O I], [O III], and [S II] lines are all quite weak. It is likely that the dense knots in 0519–69.0 have a different origin from those in the other three SNRs. Without further information, such as kinematics and elemental abundances, about the knots in 0519–69.0, we cannot confidently assess how this CSM material was ejected or has evolved. We will thus discuss below mainly knots in the other three Type Ia SNRs.

Because of the high density in the knots, their recombination time scales are short. For example, the recombination timescale is 70 yr for a density of 1000 H cm^{-3} and only 7 yr for a high density of 10,000 H cm^{-3} . Depending on the propagation of the SNR shocks, different sets of knots should brighten up and fade as time goes on, much like the knots in SN1987A’s inner ring (Fransson et al. 2015). Indeed, the *HST* H α images of N103B taken on 2013 July 11 and 2017 Jan 03 show some knots faded and some knots brightened up, as illustrated in Figure 11.

To inter-compare the knots from the Type Ia SNRs, we first examine their [S II]/H α ratio as a function of density in Figure 10. The horizontal axis is [S II] $\lambda 6716/\lambda 6731$, which is a diagnostic for electron densities. Beside the clear separation of the ISM and CSM densities, it is striking that the knots in N103B, DEM L71, and 0548–70.4 are segregated in the density distribution. N103B is the smallest and has the densest knots, while 0548–70.4 is the largest and has the least dense knots. This trend is suggestive of an evolutionary effect: as an SNR evolves and expands to larger size, its CSM knots go through ionization and shock interactions and become less dense. It is also noticeable that the greatest majority of the knots in Figure 10 follow the trend that the highest observed [S II]/H α ratio for any specific [S II] $\lambda 6716/\lambda 6731$ decreases with decreasing [S II] $\lambda 6716/\lambda 6731$, or increasing density. This trend is caused by the low critical densities of the [S II] lines, 1585 and 3981 cm^{-3} for $\lambda 6716$ and $\lambda 6731$, respectively. While the $\lambda 6716/\lambda 6731$ ratio decreases with increasing density, the [S II]/H α ratio also decreases because of increasing collisional de-excitation of the ^2D levels of S $^+$.

The [O III]/H β ratio versus [S II] $\lambda 6716/\lambda 6731$ ratio plot in Figure 9 shows contrasting distributions among the SNRs. N103B has very few knots with [O III]/H β > 2 , while DEM L71 has a significant fraction of knots with [O III]/H β > 2 . 0548–70.4, unlike N103B and DEM L71, has no knots with [O III]/H β < 0.5 . These differences may also be caused by their evolutionary status associated with the passage of SNR shocks. The large spreads of [O III]/H β ratios in 0548–70.4 and DEM L71 probably requires incomplete shocks, as suggested by the variability of some of the knots mentioned in Section 5.1.2. It is hard to get [O III]/H β above 2 or 3 except by having an incomplete recombination zone. The very low [O III]/H β ratios in some of the N103B knots (below about 0.2) sug-

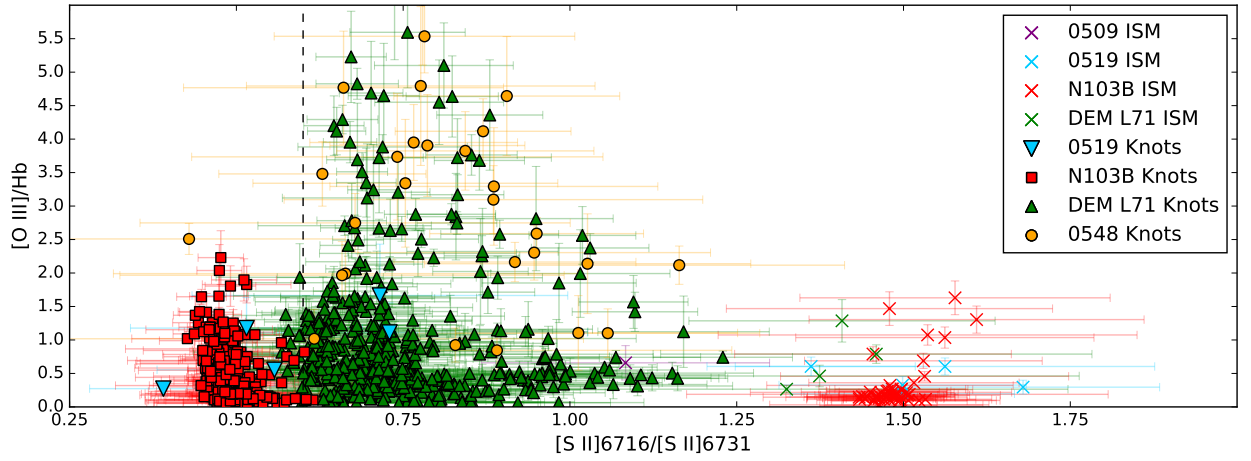


FIG. 9.— The $[\text{O III}]/\text{H}\beta$ versus $[\text{S II}]$ doublet ratio plot in and around LMC Type Ia SNRs with Balmer-dominated shells.

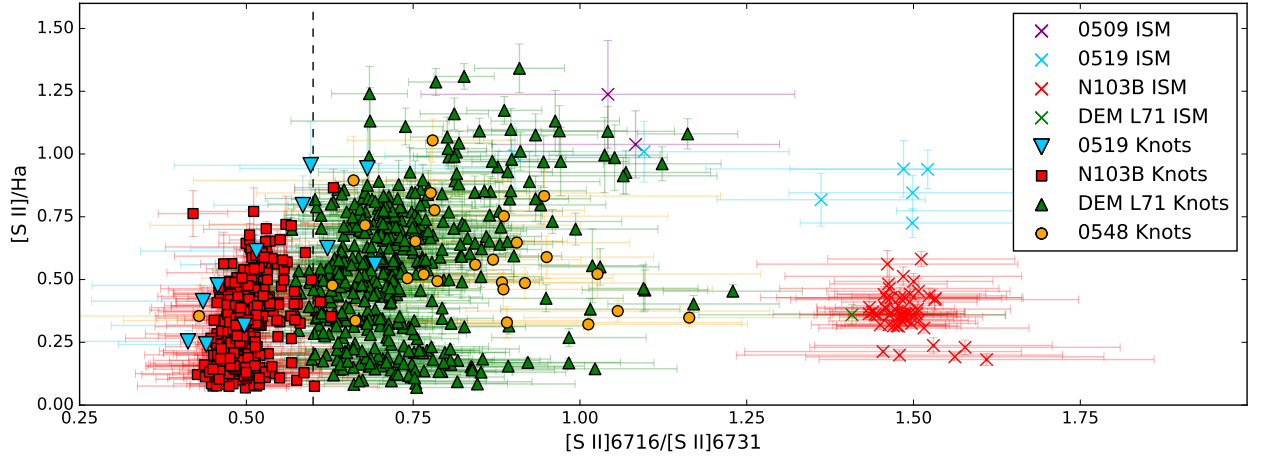


FIG. 10.— The $[\text{S II}]/\text{H}\alpha$ versus $[\text{S II}]$ doublet ratio plot in and around LMC Type Ia SNRs with Balmer-dominated shells.

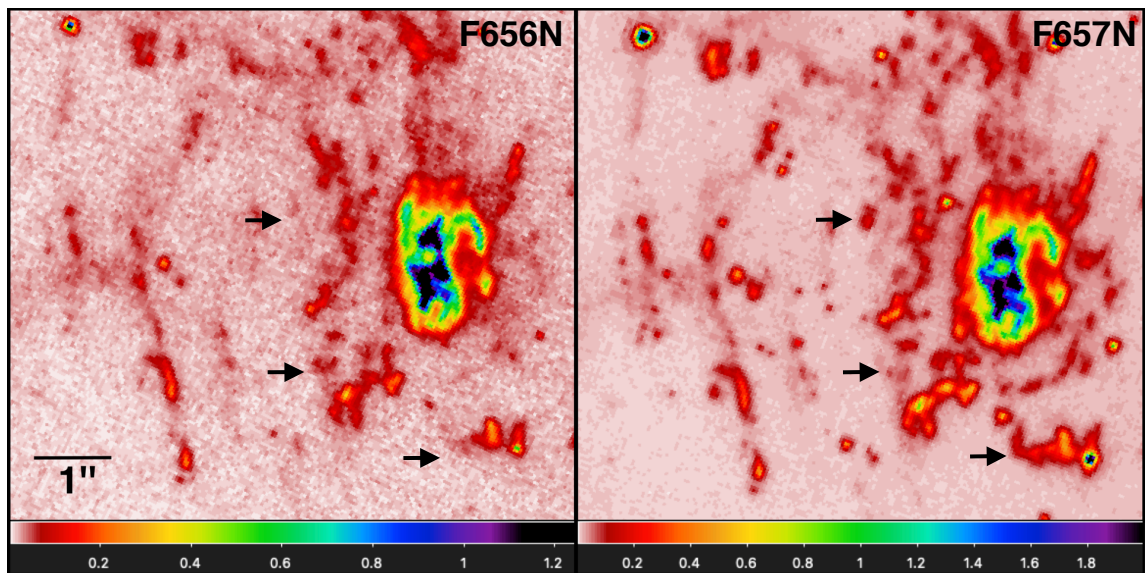


FIG. 11.— The HST $\text{H}\alpha$ images of the prominent groups of knots within N103B obtained in 2013 (left) and 2017 (right). Three knots that obviously changed brightnesses are marked by arrows.

gest very slow shocks, less than 100 km s^{-1} .

It is tempting to conclude that N103B, DEML71, and 0548–70.4 all contain dense CSM and have single-degenerate SN progenitors, although surviving companions of the progenitors have not been successfully identified (Li et al. 2019). The absence of an abundant CSM in 0509–67.5 and 0519–69.0 has been used to argue that their SN progenitors were likely of double-degenerate origin, especially since the young 0509–67.5 has no viable stellar candidate for its SN progenitor’s companion near the center of the SNR (Schaefer & Pagnotta 2012; Litke et al. 2017). However, the discovery of the knots in 0519–69.0 raises question about their origin, which may not be entirely clear at present.

5.2. Collisionless Shocks of the Balmer Shells

Both 0509–67.5 and 0519–69.0 have been well-studied: their shock speeds have been measured from HST proper motions by Hovey et al. (2018), and their ambient preshock densities have been derived from dynamical models by Seitenzahl et al. (2019). We will focus on the case of 0519–69.0 because its [O III] emission is detected and the [O III]/H β ratio has a high S/N. We adopt shock speeds of $1300\text{--}2500 \text{ km s}^{-1}$ and a preshock density of 1.5 amu cm^{-3} from the above references. We assume the hydrogen to be 50% neutral because if it were highly ionized the Balmer filaments would be correspondingly faint, and because helium atoms swept up by the shock produce enough photons to ionize at least 30% of the hydrogen. We concentrate on [O III], but generally similar considerations would apply to [S II].

Balmer line filaments show essentially pure Balmer line spectra in the optical range. The hot gas behind the shock efficiently excites neutral H atoms that pass through the shock before they can be ionized. Thus the profiles of the Balmer lines show two components: a broad component whose width is related to the postshock proton temperature and a narrow component whose width reflects the preshock temperature. For postshock temperatures of 10^6 K or more, each neutral hydrogen atom produces about 0.25 H α and about 0.05 H β photons on average before it is ionized. By comparison, there are several thousand times fewer oxygen atoms than hydrogen, so the forbidden lines that dominate most SNR shock wave spectra are expected to be faint.

Most shocks in the ISM except for C-shocks (Draine et al. 1983) are collisionless, meaning that the shock transition is governed by magnetic fields and plasma turbulence. The shock thickness is determined by the proton gyroradius or the ion skin depth, which are far smaller than the particle mean free path. Because the bulk velocities of particles entering the shock are randomized by plasma processes rather than collisions, they do not reach thermal equilibrium. Instead of Maxwellian velocity distributions, both electrons and ions can show high energy tails as a result of diffusive shock acceleration (Blandford & Eichler 1987), and different particle species can have different temperatures. In shocks faster than 1000 km s^{-1} , electron temperatures T_e are only a few percent as high as the proton temperatures T_p (Ghavamian et al. 2001, 2013), and ion temperatures T_i tend to be proportional to ion mass m_i , $T_i \sim (m_i/m_p)T_p$ (Korreck et al. 2004; Raymond et al. 2017). The collisionless nature of these shocks also explains the two-component Balmer

line profiles. Some neutrals pass through the shock unaffected, so when they are excited they produce emission with the preshock velocity profile. Others experience charge transfer with a postshock proton, and when they are excited they produce a correspondingly broad profile.

There are two possible origins for the [O III] emission. It could be produced in a narrow ionization zone just behind the shock in the same manner as the Balmer lines, or it could arise from a shock precursor. If the [O III] were produced in the shocked gas, the line would be very broad. Since there is little thermal equilibration in such fast shocks, the FWHM of the emission from 0519–69.0 would be similar to the shock speeds of 1300 km s^{-1} at the E limb and 2500 km s^{-1} at the S limb, or 25 to 60 Å. That would mean that little of the emission would be within the 8 Å band of the [O III] image, and the emission in the off-band image that is subtracted would nearly cancel out what remains.

Given an LMC oxygen to hydrogen ratio of 0.0002 to 0.0003 (Russell & Dopita 1992) and an emission rate of 0.05 H β photons per hydrogen atom, the observed [O III] to H β ratio of 0.011 would require about 0.7 [O III] photon per O atom. At very high temperatures, the number of photons is given by the ratio of excitation rate to ionization rate. We take excitation and ionization rates by electrons from CHIANTI version 8 (Dere et al. 1997; Del Zanna et al. 2015) and we assume that the excitation rate by protons is about equal to that by electrons at $T_e = (m_e/m_p)T_i$ to find that each O atom should produce 0.3 to 0.5 [O III] photons. It therefore seems that the postshock region could produce almost the observed [O III] intensity if the intensity were not spread over a band much wider than that used to generate Figure 4. We conclude that the [O III] emission in 0519–69.0 cannot come from the postshock gas.

The alternative emission region is a shock precursor. Three kinds of precursor can be present; a photoionization precursor, a cosmic ray precursor associated with diffusive shock acceleration (Blandford & Eichler 1987; Boulares & Cox 1988), or a precursor produced by broad component neutrals overtaking the shock and depositing their energy upstream (Hester et al. 1994; Morlino et al. 2012). Precursors have been inferred from H α narrow components that are broader than would be consistent with a significant neutral fraction in equilibrium, indicating that the gas is heated in a narrow precursor just ahead of the shock (Hester et al. 1994), and they can be seen as faint emission ahead of the main shock in Tycho’s SNR (Lee et al. 2010). The proton kinetic temperatures indicate narrow component widths ranging from about 3×10^4 to 10^6 K (Sollerman et al. 2003; Medina et al. 2014; Knežević et al. 2017), but the electron temperatures are poorly constrained. The precursor thickness ranges from $0.3 \times 10^{16} \text{ cm}$ to $3 \times 10^{16} \text{ cm}$ (Katsuda et al. 2016; Lee et al. 2010). Photoionization precursors associated with Balmer line filaments have been reported for Tycho’s SNR (Ghavamian et al. 2000) and the Cygnus Loop (Medina et al. 2014). The photoionization is dominated by He I and He II photons near 21 and 40 eV, respectively, and they heat the gas to around 17,000 K.

The existence of the Balmer line filaments implies a substantial neutral hydrogen fraction in the upstream

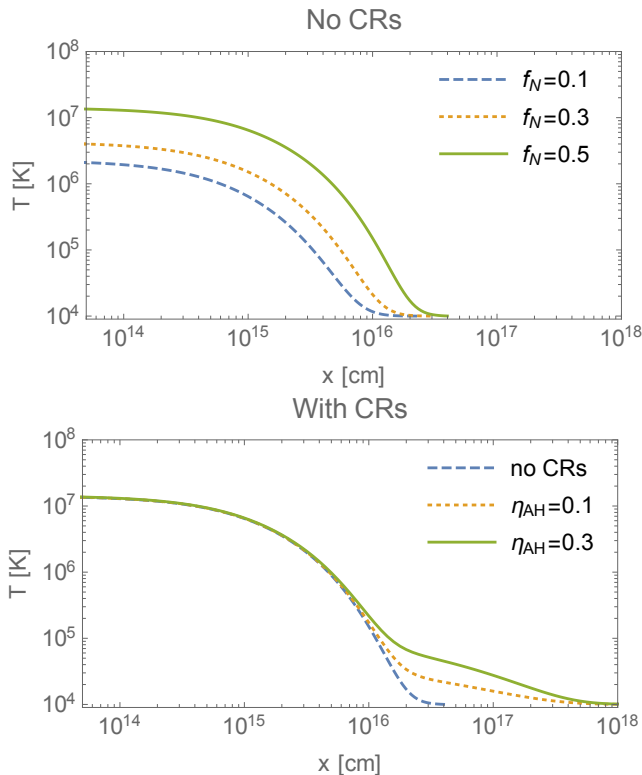


FIG. 12.— Temperature profile of protons inside the precursor with (bottom panel) and without (upper panel) cosmic rays. For all cases the assumed shock velocity is $V_{sh} = 2500 \text{ km s}^{-1}$ and the ambient density is 1.5 cm^{-3} . Upper panel: No cosmic rays. The three lines correspond to three different neutral fraction (10, 30 and 50%). Bottom panel: temperature profile assuming cosmic rays accelerated with an efficiency of $\sim 5\%$ and a neutral fraction of 50%. The two lines show the effect of changing the wave damping efficiency from 0.1 to 0.3.

gas. O III does not coexist with neutral H because of the very rapid charge transfer process $\text{H}^0 + \text{O}^{++} \rightarrow \text{H}^+ + \text{O}^+$, which has a rate coefficient of $1.0 \times 10^{-9} \text{ cm}^3 \text{ s}^{-1}$ (Kingdon & Ferland 1996). Therefore, oxygen must be ionized to O III in the precursor. It cannot be collisionally ionized, because hydrogen would be more rapidly ionized, and no neutral atoms would reach the shock to produce the $\text{H}\alpha$ broad component. However, O III can be produced by photoionization by He II $\lambda 304$ photons, because the photoionization cross section of O^+ at a photon energy of 40 eV is 30 times larger than that of H^0 (Reilman & Manson 1986). For a density of 1.5 cm^{-3} and 80% ionization, the lengths for absorption by a mixture of H and He correspond to $1''5$ and $7''$ for He I and He II photons, respectively. The latter is similar to the precursors seen in the E and S limbs of Figure 4, while the former is compatible with the thickness of the [O III] emitting region, though that may be dominated by projection effects rather than the physical thickness. The flux of He II $\lambda 304$ photons from the shock is proportional to the number of He atoms swept up per second, and therefore to the shock speed. Only shocks faster than about 1000 km s^{-1} produce enough photons to dominate over the charge transfer rate, which explains why [O III] is detected in the fastest shocks.

To evaluate the different roles of neutral and cosmic ray precursors, we calculate the temperature ahead of

the shock with and without cosmic rays acceleration. We use the model developed by Morlino et al. (2013) which allows us to calculate the shock structure in the presence of both neutral H and cosmic rays. For all cases analyzed we assumed a shock velocity of 2500 km s^{-1} and an ambient density of 1.5 cm^{-3} . Figure 12 shows the resulting temperature profile of H ions ahead of the shock. The top panel shows the cases without cosmic rays where we change the neutral fraction from 10% up to 50%. The precursor temperature increases with increasing neutral fraction as a consequence of the larger number of neutrals returning from the downstream. For a neutral fraction = 50% the precursor temperature is $\sim 10^7 \text{ K}$ hence it would be enough to efficiently excite O III. Nevertheless the precursor thickness is only $\lesssim 10^{16} \text{ cm}$ (corresponding to $0''.013$), roughly an order of magnitude smaller than the excitation lengthscale for O. Moreover, the very efficient heating by backstreaming neutrals raises the temperature to about 10^7 K , and at that temperature O III is ionized more rapidly than it is excited.

The bottom panel of the same figure shows, instead, the impact of including cosmic ray acceleration. We assume that the acceleration efficiency is only 5%, in order to be compatible with the upper limit of $\sim 7\%$ found by Hovey et al. (2018) and that the maximum energy of accelerated protons reaches $E_{\text{max}} = 1 \text{ TeV}$. Such energies can be reached if the diffusion coefficient is Bohm-like in a $\sim 1 \mu \text{ G}$ field. Notice that the maximum extent of the cosmic ray precursor corresponds to the propagation lengthscale at E_{max} , which is $l_d = D_{\text{Bohm}}(E_{\text{max}}, 1 \mu \text{ G})/V_{sh} \simeq 4 \times 10^{17} \text{ cm}$. We show two cases where the neutral fraction is fixed to 50% but the wave damping rate changes from $\eta_{AH}=0.1$ to 0.3. The parameter η_{AH} is the fraction of magnetic waves's energy (excited by cosmic rays) which is damped to thermal energy of the plasma and determines the final precursor temperature. It is worth noting that similar temperature profiles can be obtained for different combinations of acceleration efficiency, η_{AH} , E_{max} and magnetic field. But, what is important in this context is that, for reasonable values of the parameters (even for relatively small acceleration efficiency), the precursor temperature starts increasing already at a distance larger than 10^{17} cm , making possible the effective collisional excitation of O III lines.

We conclude that photoionization is responsible for the presence of O^{++} in the gas upstream of the shock, but heating by the cosmic ray precursor, and to a lesser extent by the return neutral precursor, increases the temperature and doubles the excitation rate of the [O III] transitions. For the excitation rate at temperatures of 20,000 to 40,000 K and a preshock density of 1.5 cm^{-3} , the observed [O III] flux in 0519-69.0 indicates an O III ionization fraction of around 5% to 20%. Thus all three types or precursor contribute to the observed [O III] brightness.

6. SUMMARY

Five Type Ia SNRs with Balmer-Dominated Shells are known in the LMC: 0509–67.5, 0519–69.0, N103B, DEM L71, and 0548–70.4. We have been using HST images and VLT MUSE observations of these SNRs to search for surviving companions of their SN progenitors (Litke et al. 2017; Li et al. 2017, 2019). In the course of this work, we find prevalent forbidden emission from

these Type Ia SNRs. Three types of forbidden line emission are detected: bright [O III], [O I], [S II], etc. and faint [Fe XIV] emission from shocked dense knots interior to the SNR shells, [Fe XIV] and similar high Fe ion lines from reverse shocks into the SN ejecta, and faint [O III] and other low-ionization line emission from the Balmer shells.

Small dense knots are detected in all except 0509–67.5. MUSE spectra of the knots show bright forbidden line emission from [O III], [N II], [S II], etc. Electron densities determined from the [S II] $\lambda 6716/\lambda 6731$ doublet ratio ranges from a few hundred to $\geq 10^4 \text{ cm}^{-3}$. The knots can be slightly elongated or rod-like with major-to-minor axis ratios greater than 10. As the densities exceed the critical densities of the [S II] $\lambda\lambda 6716, 6731$ lines, the [S II]/ $H\alpha$ ratio decreases at high densities and reaches as low as 0.1. The high density and small size of the knots are not characteristics of ISM; thus, the knots must have a CSM origin.

The recombination time scale for the dense knots are below 10 years, and indeed brightness variations in knots can be seen in the HST images of N103B from two epochs separated by 3.5 yr. Physical properties of the dense knots vary among the five Type Ia SNRs we studied; the variations appear to be correlated with the SNR ages (in the second column of Table 2). 0509–67.5 has no knots at all, 0519–69.0 has a small patch of knots and possibly another faint patch, N103B has the most prominent knots, DEM L71 displays knots near the shell rim, and 0548–70.4 has knots already shredded and disperse. It is conceivable that as time goes on, the CSM knots will be shocked to light up, then recombine and dissipate. The presence of CSM in Type Ia SNRs could be more

prevalent than we previously thought.

The faint [O III] line emission from the Balmer shell is detected in VLT MUSE observations of SNRs 0519–69.0, N103B, and DEM L71. The ATT WiFeS observations of 0548–70.4 have too limited spatial coverage to determine whether this SNR also has [O III] emission from its Balmer shell. We focus on the case of 0519–69.0 because its [O III] emission is well-measured and its shock velocity and ambient ISM density have been studied in detail and reported by Hovey et al. (2018) and Seitzenzahl et al. (2019). We exclude the postshock origin of the [O III] emission because its FWHM is not compatible with the broad component of the Balmer lines. For the preshock origin, we considered three possibilities: photoionization precursor, cosmic ray precursor, and neutral precursor. With considerations of the [O III]/ $H\beta$ ratio and thickness of the [O III] shell, we conclude that the [O III] emission arises from oxygen that has been photoionized by [He II] $\lambda 304$ photons and is then collisionally excited in a shock precursor heated mainly by cosmic rays. A more detailed quantitative analysis of the nebular lines in these Type Ia SNRs will be carried out and reported in a future paper.

Y.-H.C. and C.-J.L. are supported by Taiwanese Ministry of Science and Technology grant MOST 108-2811-M-001-587, 109-2112-M-001-040, and 109-2811-M-001-545.

Software: SAOImage DS9 (Joye & Mandel 2003), QFitsView (Ott 2012), astropy (Astropy Collaboration et al. 2018), matplotlib (Hunter 2007), numpy (van der Walt et al. 2011; Harris et al. 2020), scipy (Virtanen et al. 2020)

APPENDIX

REFERENCES

- Astropy Collaboration, Price-Whelan, A. M., Sipőcz, B. M., et al. 2018, *AJ*, 156, 123. doi:10.3847/1538-3881/aabc4f
- Blair, W. P., Long, K. S., & Vancura, O. 1991, *ApJ*, 366, 484
- Blair, W. P., Ghavamian, P., Raymond, J. C., et al. 2020, *ApJ*, 902, 153. doi:10.3847/1538-4357/abb3c7
- Blandford, R. & Eichler, D. 1987, *Phys. Rep.*, 154, 1
- Boulares, A. & Cox, D. P. 1988, *ApJ*, 333, 198
- Chevalier, R. A., Kirshner, R. P., & Raymond, J. C. 1980, *ApJ*, 235, 186
- Chu, Y.-H., Caulet, A., Dickel, J., et al. 1999, *New Views of the Magellanic Clouds*, 190, 143
- Del Zanna, G., Dere, K. P., Young, P. R., et al. 2015, *A&A*, 582, A56
- Dere, K. P., Landi, E., Mason, H. E., et al. 1997, *A&AS*, 125, 149
- Dopita, M. A., Vogt, F. P. A., Sutherland, R. S., et al. 2018, *ApJS*, 237, 10. doi:10.3847/1538-4365/aac837
- Dopita, M. A., Seitzenzahl, I. R., Sutherland, R. S., et al. 2019, *AJ*, 157, 50. doi:10.3847/1538-3881/aaf235
- Draine, B. T., Roberge, W. G., & Dalgarno, A. 1983, *ApJ*, 264, 485
- Fesen, R. A., Becker, R. H., Blair, W. P., et al. 1989, *ApJ*, 338, L13
- Fransson, C., Larsson, J., Migotto, K., et al. 2015, *ApJ*, 806, L19. doi:10.1088/2041-8205/806/1/L19
- Ghavamian, P., Raymond, J., Hartigan, P., et al. 2000, *ApJ*, 535, 266
- Ghavamian, P., Raymond, J., Smith, R. C., et al. 2001, *ApJ*, 547, 995
- Ghavamian, P., Rakowski, C. E., Hughes, J. P., & Williams, T. B. 2003, *ApJ*, 590, 833
- Ghavamian, P., Schwartz, S. J., Mitchell, J., et al. 2013, *Space Sci. Rev.*, 178, 633
- Ghavamian, P., Seitzenzahl, I. R., Vogt, F. P. A., et al. 2017, *ApJ*, 847, 122
- Harris, C. R., Millman, K. J., van der Walt, S. J., et al. 2020, *Nature*, 585, 357. doi:10.1038/s41586-020-2649-2
- Hendrick, S. P., Borkowski, K. J., & Reynolds, S. P. 2003, *ApJ*, 593, 370
- Heng, K. 2010, *PASA*, 27, 23
- Hester, J. J., Raymond, J. C., & Blair, W. P. 1994, *ApJ*, 420, 721. doi:10.1086/173598
- Hovey, L., Hughes, J. P., & Eriksen, K. 2015, *ApJ*, 809, 119
- Hovey, L., Hughes, J. P., McCully, C., et al. 2018, *ApJ*, 862, 148
- Hunter, J. D. 2007, *Computing in Science and Engineering*, 9, 90. doi:10.1109/MCSE.2007.55
- Joye, W. A. & Mandel, E. 2003, *Astronomical Data Analysis Software and Systems XII*, 295, 489
- Katsuda, S., Maeda, K., Ohira, Y., et al. 2016, *ApJ*, 819, L32
- Kingdon, J. B. & Ferland, G. J. 1996, *ApJS*, 106, 205. doi:10.1086/192335
- Kirshner R. P. & Chevalier, R. A. 1978, *A&A*, 67, 267
- Knežević, S., Läsker, R., van de Ven, G., et al. 2017, *ApJ*, 846, 167
- Korreck, K. E., Raymond, J. C., Zurbuchen, T. H., et al. 2004, *ApJ*, 615, 280
- Lee, J.-J., Raymond, J. C., Park, S., et al. 2010, *ApJ*, 715, L146
- Li, C.-J., Chu, Y.-H., Gruendl, R. A., et al. 2017, *ApJ*, 836, 85
- Li, C.-J., Kerzendorf, W. E., Chu, Y.-H., et al. 2019, *ApJ*, 886, 99
- Litke, K. C., Chu, Y.-H., Holmes, A., et al. 2017, *ApJ*, 837, 111
- Long K. S., & Blair, W. P. 1990, *ApJ*, 358, L13
- Mattila, S., Lundqvist, P., Grönningsson, P., et al. 2010, *ApJ*, 717, 1140. doi:10.1088/0004-637X/717/2/1140
- Medina, A. A., Raymond, J. C., Edgar, R. J., et al. 2014, *ApJ*, 791, 30
- Morlino, G., Bandiera, R., Blasi, P., et al. 2012, *ApJ*, 760, 137
- Morlino, G., Blasi, P., Bandiera, R., et al. 2013, *ApJ*, 768, 148. doi:10.1088/0004-637X/768/2/148
- Ott, T. 2012, *Astrophysics Source Code Library*. ascl:1210.019

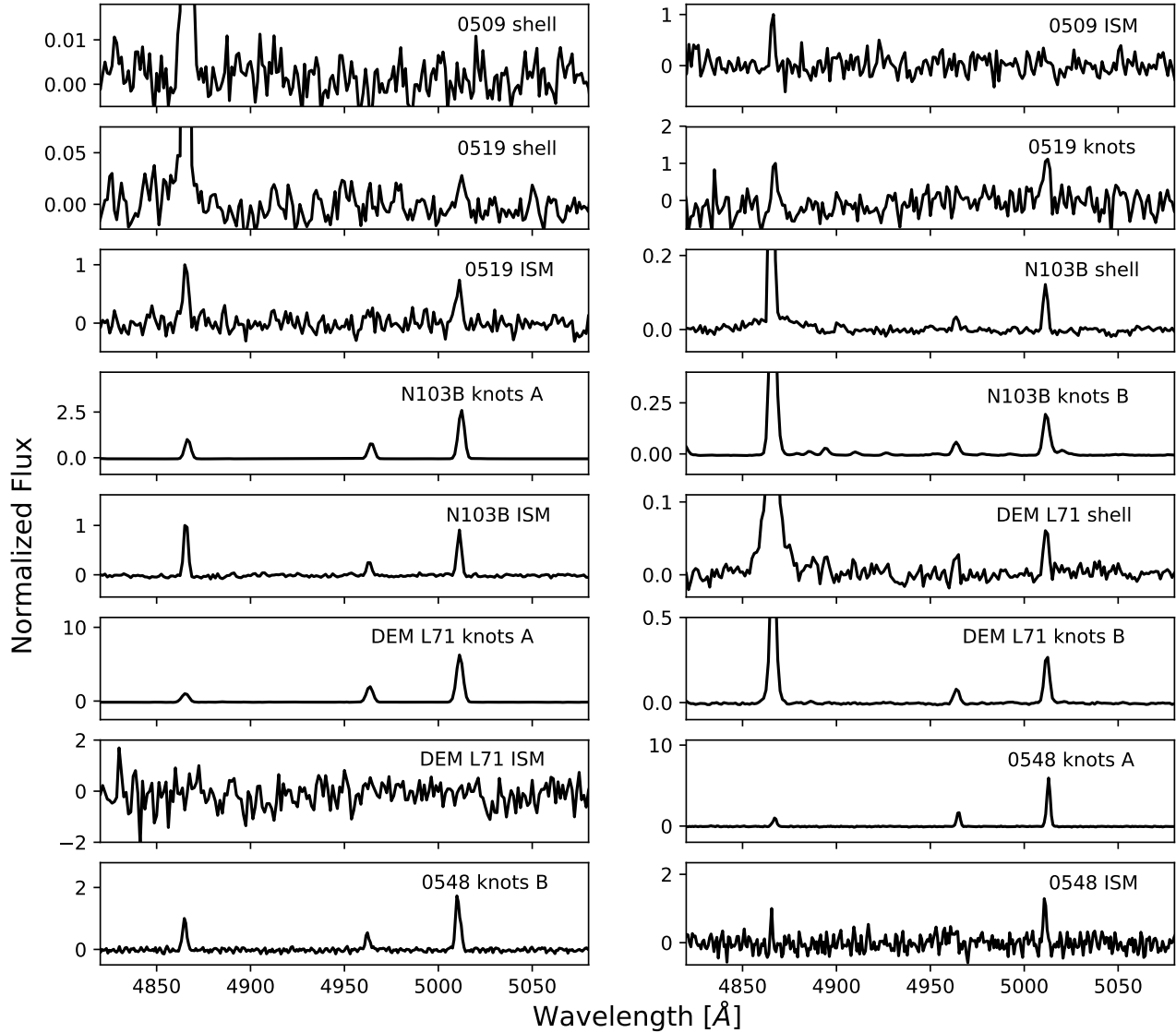


FIG. 13.— The spectra obtained from VLT MUSE and ATT WiFeS observations showing the representative $[\text{O III}]/\text{H}\beta$ ratios in and around SNRs with Balmer-dominated shells. In each panel, all emission lines fluxes are normalized to the $\text{H}\beta$ line. Knots A and B are examples with contrasting $[\text{O III}]/\text{H}\beta$ ratios.

Raymond, J. C., Blair, W. P., Fesen, R. A., & Gull, T. R. 1983, *ApJ*, 275, 636
 Raymond, J. C., Winkler, P. F., Blair, W. P., et al. 2017, *ApJ*, 851, 12
 Reilman, R. F. & Manson, S. T. 1986, *ApJS*, 62, 939. doi:10.1086/191162
 Rest, A., Suntzeff, N. B., Olsen, K., et al. 2005, *Nature*, 438, 1132
 Russell, S. C. & Dopita, M. A. 1992, *ApJ*, 384, 508. doi:10.1086/170893
 Sankrit, R., Blair, W. P., Frattare, L. M., et al. 2008, *AJ*, 135, 538
 Sano, H., Matsumura, H., Nagaya, T., et al. 2019, *ApJ*, 873, 40. doi:10.3847/1538-4357/ab02fd
 Sano, H., Plucinsky, P. P., Bamba, A., et al. 2020, *ApJ*, 902, 53. doi:10.3847/1538-4357/abb469
 Schaefer, B. E., & Pagnotta, A. 2012, *Nature*, 481, 164
 Schweizer F. & Lasker, B. M. 1978, *ApJ*, 226, 167

Seitzzahl, I. R., Ghavamian, P., Laming, J. M., et al. 2019, *Phys. Rev. Lett.*, 123, 041101
 Smith, R. C., Kirshner, R. P., Blair, W. P., & Winkler, P. F. 1991, *ApJ*, 375, 652
 Sollerman, J., Ghavamian, P., Lundqvist, P., et al. 2003, *A&A*, 407, 249
 Tuohy, I. R., Dopita, M. A., Mathewson, D. S., Long, K. S., & Helfand, D. J. 1982, *ApJ*, 261, 473
 van der Walt, S., Colbert, S. C., & Varoquaux, G. 2011, *Computing in Science and Engineering*, 13, 22. doi:10.1109/MCSE.2011.37
 Virtanen, P., Gommers, R., Oliphant, T. E., et al. 2020, *Nature Methods*, 17, 261. doi:10.1038/s41592-019-0686-2
 Weilbacher, P. M., Streicher, O., Urrutia, T., et al. 2014, in *ASP Conf. Ser.*, Vol. 485, *Astronomical Data Analysis Software and Systems XXIII*, ed. N. Manset & P. Forshay, 451
 Williams, B. J., Borkowski, K. J., Reynolds, S. P., et al. 2014, *ApJ*, 790, 139

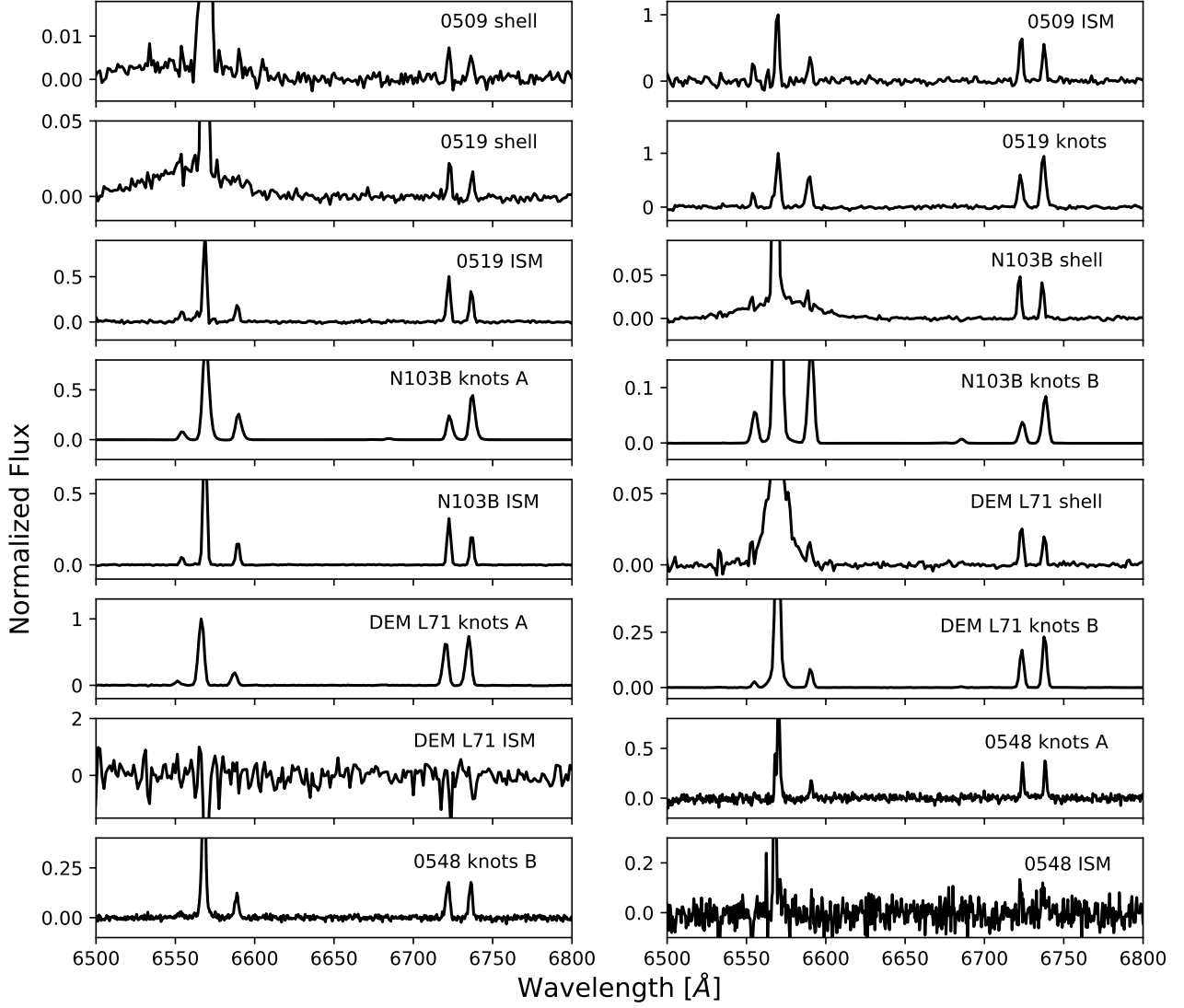


FIG. 14.— The spectra obtained from VLT MUSE and ATT WiFeS observations showing the representative $[S\ II]/H\alpha$ ratios in and around SNRs with Balmer-dominated shells. In each panel, all emission lines fluxes are normalized to the $H\alpha$ line. Knots A and B are examples with contrasting $[S\ II]/H\alpha$ ratios.